Modeling CO_2-Brine-Rock Interaction Including Mercury and H_2S Impurities in the Context of CO_2 Geologic Storage

Nicolas Spycher[1]

Curtis M. Oldenburg[2]

Earth Sciences Division
Lawrence Berkeley National Laboratory

January 27, 2014

[1]nspycher@lbl.gov [2]cmoldenburg@lbl.gov

This page left intentionally blank.

ABSTRACT

This study uses modeling and simulation approaches to investigate the impacts on injectivity of trace amounts of mercury (Hg) in a carbon dioxide (CO_2) stream injected for geologic carbon sequestration in a sandstone reservoir at ~2.5 km depth. At the range of Hg concentrations expected (7-190 ppbV, or ~ 0.06-1.6 mg/std.m^3CO_2), the total volumetric plugging that could occur due to complete condensation of Hg, or due to complete precipitation of Hg as cinnabar, results in a very small porosity change. In addition, Hg concentration much higher than the concentrations considered here would be required for Hg condensation to even occur. Concentration of aqueous Hg by water evaporation into CO_2 is also unlikely because the higher volatility of Hg relative to H_2O at reservoir conditions prevents the Hg concentration from increasing in groundwater as dry CO_2 sweeps through, volatilizing both H_2O and Hg. Using a model-derived aqueous solution to represent the formation water, batch reactive geochemical modeling show that the reaction of the formation water with the CO_2-Hg mixture causes the pH to drop to about 4.7 and then become buffered near 5.2 upon reaction with the sediments, with a negligible net volume change from mineral dissolution and precipitation. Cinnabar (HgS(s)) is found to be thermodynamically stable as soon as the Hg-bearing CO_2 reacts with the formation water which contains small amounts of dissolved sulfide. Liquid mercury (Hg(l)) is not found to be thermodynamically stable at any point during the simulation. Two-dimensional radial reactive transport simulations of CO_2 injection at a rate of 14.8 kg/s into a 400 m-thick formation at isothermal conditions of 106°C and average pressure near 215 bar, with varying amounts of Hg and H_2S trace gases, show generally that porosity changes only by about ±0.05% (absolute, i.e., new porosity = initial porosity ±0.0005) with Hg predicted to readily precipitate from the CO_2 as cinnabar in a zone mostly matching the single-phase CO_2 plume. The precipitation of minerals other than cinnabar, however, dominates the evolution of porosity. Main reactions include the replacement of primarily Fe-chlorite by siderite, of calcite by dolomite, and of K-feldspar by muscovite. Chalcedony is also predicted to precipitate from the dissolution of feldspars and quartz. Although the range of predicted porosity change is quite small, the amount of dissolution and precipitation predicted for these individual minerals is not negligible. These reactive transport simulations assume that Hg gas behaves ideally. To examine effects of non-ideality on these simulations, approximate calculations of the fugacity coefficient of Hg in CO_2 were made. Results suggest that Hg condensation could be significantly overestimated when assuming ideal gas behavior, making our simulation results conservative with respect to impacts on injectivity. The effect of pressure on Henry's constant for Hg is estimated to yield Hg solubilities about 10% lower than when this effect is not considered, a change that is considered too small to affect the conclusions of this report. Although all results in this study are based on relatively mature data and modeling approaches, in the absence of experimental data and more detailed site-specific information, it is not possible to fully validate the results and conclusions.

This page left intentionally blank.

TABLE OF CONTENTS

LIST OF FIGURES

LIST OF TABLES

EXECUTIVE SUMMARY

This study investigates the injection of carbon dioxide (CO_2) with mercury (Hg) co-contaminant at concentrations of 7-190 ppbV (~ 0.06-1.6 mg/std.$m^3$$CO_2$) into a sandstone aquifer targeted for geologic carbon sequestration using various modeling and computational approaches. The main objective of the study is to assess the potential for Hg precipitation and/or condensation within the targeted formation with particular focus on impacts to injectivity through porosity and permeability changes. The effects of trace H_2S concentrations at 200 ppmV in the CO_2-Hg mixture are also investigated. The study considers injection at a rate of about 15 kg/s CO_2 through an injector with a 300 m-long perforated interval into the reservoir which is at a depth of approximately 2.5 km at pressure and temperature conditions of ~215 bar (3120 psi) and 106°C (223°F).

Following a short introduction in Section 1, simple calculations are presented in Section 2 to evaluate the amount and volume of Hg injected with the CO_2 to assess approximately the volumetric distribution of Hg and CO_2 in the storage reservoir, as well as potential effects on porosity. Analytical calculations are also performed to assess the potential for Hg to condense from the gas phase. The potential for evaporative concentration of aqueous Hg by prolonged injection of CO_2 is then investigated using analytical methods and a numerical model. Results indicate that the porosity change would be insignificant if Hg condensed as liquid mercury, or precipitated as cinnabar (HgS), over scales of meters to tens of meters away from the injector. Also, a Hg concentration much higher than the concentrations considered here would be required for condensation to even occur. As for evaporative concentration, the relatively higher volatility of Hg relative to H_2O means that Hg will not concentrate in groundwater as dry CO_2 sweeps through volatilizing both H_2O and Hg.

In Section 3, the mineralogy of the reservoir formation is assessed, and the composition of the deep (in-situ) formation water is reconstructed by geochemical modeling. In order to establish the background conditions for the complex reactive transport simulations presented in Section 4, the chemical reactions between formation water, sediments, and a CO_2+Hg mixture are simulated first using a thermodynamic model that does not consider transport. Results indicate that the pH of the formation water initially drops to about 4.7 from the carbonic acid released by the dissolution of CO_2. The pH then becomes buffered near 5.2 upon reaction with the sediments. The main reaction products are chalcedony forming from feldspar and quartz dissolution, and siderite primarily from Fe-chlorite dissolution. The net volume change from mineral dissolution and precipitation is negligible. Cinnabar (HgS(s)) is found to be thermodynamically stable as soon as the Hg-bearing CO_2 reacts with the formation water, which contains small amounts of dissolved sulfide. Liquid mercury (Hg(l)) is not found to be thermodynamically stable at any point during the simulation. The dissolved Hg concentration is very small (on the order of several ppb).

In Section 4, results of reactive transport simulations are presented. The injection of Hg- and H_2S-bearing CO_2 into a deep sandstone formation is simulated, with focus on the spatial distribution of Hg deposition and the porosity change around the injection well. The model is set up as a two-dimensional radial X-Z domain. Injection is simulated for a period of 40 years at a constant CO_2 injection rate of 14.8 kg/s into a 400 m-thick formation at isothermal conditions of 106°C and average pressure near 215 bar. Three cases of injection are simulated, with CO_2

containing: (1) 200 ppmV H_2S and 190 ppbV Hg, (2) no H_2S and 190 ppbV Hg, and (3) 200 ppmV H_2S and 7 ppbV Hg. These simulations yield similar results. Porosity is predicted to change only by about ±0.05% (absolute, i.e., new porosity = initial porosity ±0.0005). Mercury is predicted to readily precipitate from the CO_2 as cinnabar in a zone mostly matching the single-phase CO_2 plume, and resulting in a negligible porosity decrease (about 0.005% absolute for the higher Hg concentration, and about 100 times less for the low-concentration case). The dissolved Hg concentrations remain mostly less than 8 ppb. Supercritical CO_2 is predicted to migrate to about 2100 m from the injection well, however the single-phase CO_2 zone remains within about 60 m of the injection well. The pH of the formation water is predicted to drop to ~4.5–5 near the well, and to ~5–6 farther away in a zone initially invaded by CO_2 but where CO_2 eventually fully disappears by dissolution and buoyancy flow. The main reactions include the replacement of primarily Fe-chlorite by siderite, of calcite by dolomite, and of K-feldspar by muscovite, and precipitation of chalcedony. H_2S is quite soluble in water (much more than CO_2), and essentially fully dissolves at first contact with the formation water when it is present in the injected CO_2. The computations in this study are based on the assumption of ideal gas behavior for Hg. The effect of this assumption on model results is evaluated in Section 5. Very approximate calculations are presented to estimate the fugacity coefficient of Hg in CO_2 at the temperature and pressure of interest. Results suggest that Hg precipitation could be significantly overestimated when assuming ideal gas behavior. This implies that the model results presented here are very likely conservative, i.e., they overestimate the amount of precipitation of minerals containing Hg. The effect of pressure on Henry's constant for Hg is also evaluated. This effect is estimated to yield Hg solubility about 10% lower than when this effect is not considered, a change that is considered too small to affect the conclusions of this report.

All of the modeling and calculation approaches applied in this study suggest that liquid Hg will not form, but that the precipitation of small amounts of cinnabar is expected. Modeling results suggest that such precipitation will have a negligible effect on porosity because cinnabar is precipitated over a large area with homogenous properties. An appreciable porosity reduction would only be expected if all of the Hg precipitated over regions at the centimeter scale. Because of the significant length of the perforated interval, we speculate that even if precipitation occurred in some region near the well resulting in significant permeability decrease, other regions of the reservoir along the perforated interval would remain available to accommodate the injection rate. Although all results in this study are based on relatively mature data and modeling approaches, in the absence of experimental data and more detailed site-specific information, it is not possible to fully validate the results and conclusions.

1 INTRODUCTION

Mercury (Hg) is found naturally in many oil and gas fields, where it is present in trace quantities and most frequently detected in elemental form (e.g., Zettlizer et al., 1997; Eckersley, 2010). The presence of Hg in hydrocarbon production streams can be detrimental because Hg forms amalgams with various metals (e.g., Al, Cu, Zn, Ni, Fe, brass), which can weaken these metals (e.g., Bingham, 1990). This phenomenon is commonly referred to as liquid metal embrittlement (LME) (Joseph et al., 1999). An example of such detrimental effect is the severe damage that Hg can cause to aluminum heat exchangers (e.g., Eckersley, 2010). Mercury can also poison catalysts, and its amalgamation in pipes and various equipment components can result in the designation of contaminated materials as hazardous waste (Weatherford Laboratories, 2011). For these reasons, Hg is typically removed from production streams using various separation techniques (e.g., Markovs and Clark, 2005; Eckersley, 2010).

With the prospect of geologic carbon dioxide sequestration (GCS) being used as an approach to reduce greenhouse gas emissions, concern has arisen about the effects of Hg injected as a contaminant in CO_2 separated from natural gas production streams that contain Hg. Following amine separation of CO_2 from natural gas containing Hg, captured CO_2 can contain significant amounts of Hg (in the mg/m^3 range, or 100 ppbV range; Cui et al., 2010). Complete removal of Hg from the captured CO_2 is either unachievable or prohibitively expensive.

In this study, we investigated the effects of the injection of CO_2 with Hg co-contaminant on a sandstone aquifer. The co-injection of small quantities of Hg (7–190 ppbV) with CO_2 into a deep sandstone geologic formation is considered under specific conditions relevant to an actual injection site. The main objective is to assess the Hg geochemical behavior upon reinjection, with a particular emphasis on potential permeability reduction caused by Hg precipitation and/or condensation within the targeted geologic formation. Because H_2S is another impurity typically difficult to entirely remove from natural gas and from the captured CO_2, and because Hg exhibits a strong affinity for sulfide, the effect of trace H_2S concentrations (200 ppmV) in the CO_2 was also investigated.

This study is purely computational, and relies on various numerical simulations performed in order of increasing complexity. General input data were taken from the literature when available, along with some limited data appropriate for a particular (unnamed) site. Although these various technical analyses were conducted for the unnamed injection location, the results are relevant generally to similar sandstone reservoirs being considered for geologic carbon sequestration of CO_2 captured from Hg-containing natural gas.

2 PRELIMINARY ANALYSES

Site-specific injection conditions and some reference data used in calculations are discussed first (Section 2.1). Prior to conducting the main numerical modeling analyses, simpler calculations were made to evaluate the amount and volume of Hg injected with CO_2, and to assess in a very approximate manner the volumetric distribution of Hg and CO_2 within the target formation, and potential effects on porosity (Section 2.2). Simple dew point calculations were also performed to assess the potential for gaseous Hg (in the CO_2) to condense from the CO_2 (Section 2.3). Because small quantities of water are known to evaporate into compressed CO_2 (e.g., Pruess and Müller, 2009), the potential for such evaporation to concentrate aqueous Hg upon prolonged injection of CO_2 was also investigated using simple analytical derivations and numerical modeling analyses (Section 2.4).

2.1 Injection Specifications and Reference Data

The basic problem specification including CO_2 injection rates, total number of injectors, Hg concentration, and typical operating pressure and temperature conditions are shown in Table 2-1. These specifications apply to an unnamed target formation, and serve as a basis for computations presented in this report. Basic physicochemical data necessary for the preliminary analyses discussed in this section are also listed in Table 2-1, along with their sources.

Table 2-1. *Operational and reference data*

Variable	Value	Units	Source
Operational Data:			
Temperature	106	(C)	1
Pressure	3125	(psia)	1
	215	(bar)	
Total CO_2 injection rate	2.20E+08	(std ft^3/d)	1
Number of injectors	9		1
CO_2 injection rate per injector	2.53E+08	(std m^3/y)	
	14.8	(kg/s)	
Injection time period	40	(y)	1
Hg concentration in CO_2	1.58	(mg/m^3)	1
	0.19	(ppmV)	
H_2S concentration in CO_2	200	(ppmV)	1
Reference Data:			
CO_2 density (std conditions, 15C, 1bar)	1.848	(kg/m^3)	2
CO_2 density (reservoir, 106°C, 215 bar)	490.5	(kg/m^3)	2
Hg(l) density (20°C, 1 bar)*	13,546	(kg/m^3)	3
HgS(s) density (25°C, 1 bar)*	8,176	(kg/m^3)	5
CO_2 molecular weight	44.0095	(g/mol)	4
Hg(l) molecular weight	200.59	(g/mol)	4
HgS(s) molecular weight	232.66	(g/mol)	4

* Minimal temperature and pressure effect not considered here

Source: 1 Site operator (pers. comm.); 2 Altunin (1975); 3 Holman and ten Seldam (1994); 4 NIST (2011); 5 Mindat.org (http://www.mindat.org/min-1052.html, last accessed 12/12/2013).

2.2 Inventory/Mass-balance Calculations

Approximate volumes of injected CO_2 and Hg were calculated given specific assumptions (Table 2-2) and injection conditions (Table 2-1). It is assumed that all Hg initially in the CO_2 is deposited in the target formation, either as condensed elemental liquid mercury (Hg(l)) or as precipitated cinnabar (HgS(s)), which is known to readily form in the presence of sulfide and has an extremely low solubility. The calculated Hg mass flow rate into the target formation is non-negligible (400 kg/y, Table 2-2). However, the corresponding (maximum) Hg volume that could precipitate upon injection is quite small relative to the huge volume of injected supercritical CO_2. This is the result of the high densities of Hg(l) and HgS(s) relative to the density of supercritical CO_2 at the pressure and temperature of interest (Table 2-1). Note that the change in Hg(l) and HgS(s) density with temperature and pressure is not considered here, because it is small and is considered a second-order effect. Given these approximate calculations, it is evident that a significant reduction in permeability from Hg deposition would require precipitation within a small and localized portion of the reservoir.

If Hg deposition occurred directly around the injector, using the volumes and assumptions shown in Tables 2-1 and 2-2, and further assuming homogenous radial Hg deposition around a 10-inch injector well, it is possible to roughly estimate the lateral extent of Hg precipitation around the well versus porosity drop, or vice versa. In doing so, it is estimated that an absolute porosity drop of more than 1% would require precipitation of all injected Hg within less than ~0.2–0.4 m from the injection well (Figure 2-1). It will be shown later in this report, using numerical simulations, that the distribution of CO_2 and Hg around the injection well cannot be assumed to be cylindrical in shape, because the buoyancy of supercritical CO_2 results in a more upward-widening conical plume. Nevertheless, these approximate calculations suggest that very small porosity changes would occur if Hg precipitated over scales of meters to tens of meters away from the injector, a finding that falls in line with the results of numerical simulations presented later (Section 4).

Table 2-2. *Approximate Hg and CO_2 volumetric data calculated using assumptions and data shown in Table 2-1.*

Variable	Value	Units
Assumptions		
Injection time period	40	(y)
Porosity	0.15	
Residual CO_2 saturation	0.4	
Thickness of injection interval	300	(m)
Hg mass and volumetric rates[1]		
Mass rate	399	(kg/y)
Volumetric rate as Hg(l)	0.0295	(m^3/y)
Volumetric rate as HgS(s)	0.0489	(m^3/y)
Cumulative volumetric data[1,2]		
Reservoir volume with residual CO_2	6.35E+08	(m^3)
Total Hg volume as Hg(l)	1.18	(m^3)
Total Hg volume as HgS(s)	1.95	(m^3)
Radius of CO_2 plume	821	(m)

[1]Per injector; [2]Assuming a cylindrical plume centered on the injector at residual saturation shown.

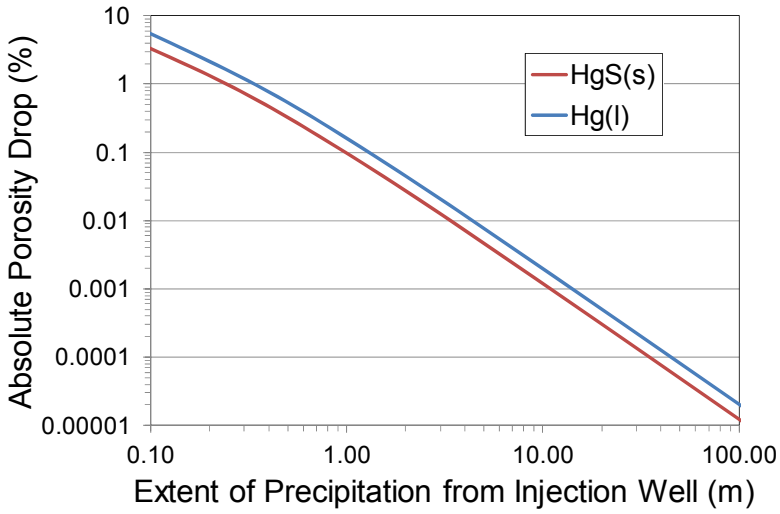

Figure 2-1. *Absolute porosity change estimated for a given extent of homogenous Hg deposition radially around an injector well (see Tables 2.1 and 2.2 for assumptions and inputs).*

2.3 Potential for Hg Condensation

The potential for Hg condensation from the supercritical CO_2 phase as Hg(l) (liquid elemental mercury) was investigated by applying simple dew-point calculations using Hg vapor-pressure data from the literature. These approximate calculations were done without considering non-ideal mixing effects between Hg and CO_2. Such effects are discussed later in this report (Section 5).

Two sources of Hg vapor-pressure data were considered. The main reference data were taken from Huber et al. (2006), who presented a correlation (their Equation 4) to compute vapor pressure as a function of temperature, which they fitted to a large number of experimental data points from the literature. The results of this correlation were also compared to Hg vapor pressures computed from equilibrium constants (as a function of temperature) for the reaction Hg(v) ↔ Hg(l) derived by Spycher and Reed (1989) using published Gibbs free energy data. These latter data were used for the geochemical and reactive transport numerical analyses presented later in this report, and are found to compare reasonably well at low temperatures with the more recent data from Huber et al. (2006), but start departing at higher temperatures of interest here (106°C) (Figure 2-2a), with the data from Spycher and Reed (1989) showing a saturation pressure about 26% lower than that given by Huber et al. (2006), reflecting a significant variability in published experimental data.

The potential for Hg(l) condensation from the supercritical CO_2 phase was evaluated in a manner analogous to the calculation of air relative humidity. The "relative humidity" of Hg in CO_2, under ideal conditions, can be expressed by

$$RH = P_{Hg}/P_{satHg} = y_{Hg}\, P_{tot} / P_{satHg} \qquad (2\text{-}1)$$

where RH stands for "relative humidity," P_{Hg} is the partial pressure of Hg in the CO_2, P_{satHg} is the saturation pressure of Hg, P_{tot} is the total system pressure, and y_{Hg} is the mole fraction of Hg in CO_2. At 106°C the Hg saturation pressure is about 51×10^{-5} bar (Huber et al., 2006; Figure 2.2). Using Eq. 2-1 with this value, a Hg mole fraction of 190×10^{-9} (corresponding to 190 ppbV, Table 2-1, because of equality of mole and volume fractions), and at a total system pressure of 213 bar, a "relative humidity" value of about 0.08 is obtained. This value is more than one order of magnitude below the theoretical dew point (at RH = 1), suggesting that condensation is highly unlikely, which is also supported by the numerical simulations presented later.

By setting RH equal to 1 in Eq. 2-1 and solving for y_{Hg} given a total system pressure (213 bar), and Hg vapor pressure (as a function of temperature) from the sources discussed above, this equation can also be used to estimate the concentration of Hg in the gas phase required for condensation to occur (i.e., the saturation concentration). These calculations show (Figure 2-2b) that an Hg concentration much higher than the concentration considered here (~190 ppbV) would be required for condensation to occur.

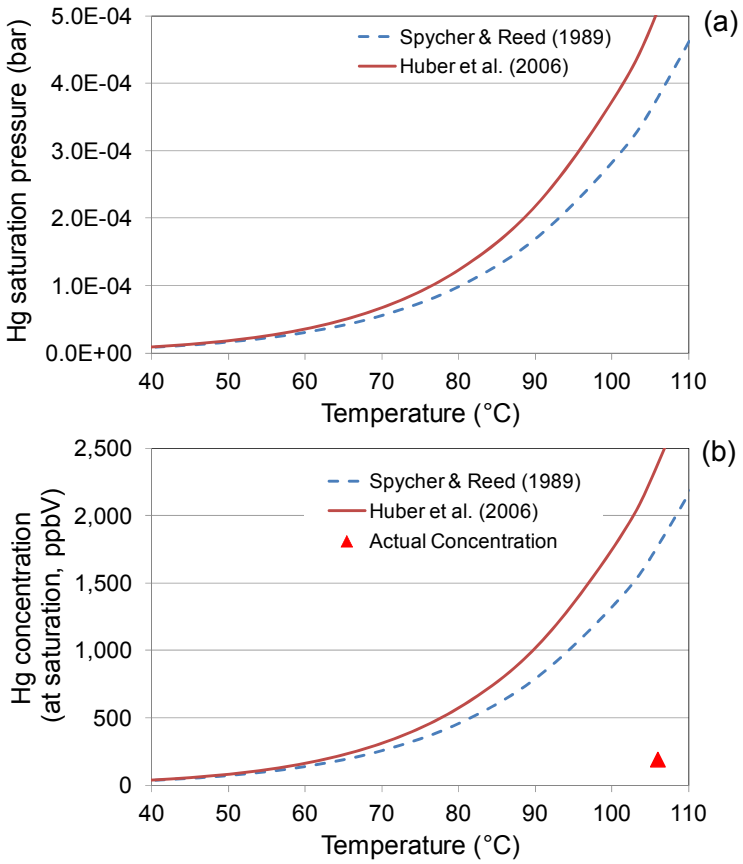

Figure 2-2. *Hg saturation pressure (a), and saturation concentration at 213 bar (b) (assuming ideal gas behavior). The actual Hg concentration is significantly below the saturation level.*

2.4 Potential for Hg Evaporative Concentration

Because small quantities of water can evaporate into dry supercritical CO_2, the prolonged flux of supercritical CO_2 into brine in an aquifer can result in evaporative concentration of the brine constituents and salt precipitation (e.g., Pruess and Müller, 2009). The question arises, then, about the possibility of such evaporation to concentrate any aqueous Hg that could have dissolved from the CO_2 phase into the formation brine. Because Hg partitions in both aqueous and gas phases, the answer to this question involves the relative volatility of Hg and water. Assuming ideal behavior, the partitioning of the volatile solute (Hg in this case) between the aqueous and gas phases can be expressed using Henry's law

$$Kh = P_{Hg} / x_{Hg} \tag{2-2}$$

where P_{Hg} and x_{Hg} respectively stand for partial pressure and mole fraction of Hg in the solvent (water) and Kh is the Henry's law constant. In contrast, the partitioning of the solvent (ideal H_2O in this case) can be expressed using Raoult's law

$$P_{satH2O} = P_{H2O} / x_{H2O} \tag{2-3}$$

where P_{H2O} and P_{satH2O} stand for, respectively, the actual pressure and the saturation pressure of H_2O vapor, and x_{H2O} is the water mole fraction. Using these equations in combination with a mass balance expressing the constant total amount of each component in aqueous+gas phases, it can be shown that the concentration factor of Hg in the aqueous phase, *cfact*, takes the form

$$cfact = 1 / \{ kgw + (Kh / P_{satH2O}) (1 - kgw) \} \quad (2\text{-}4)$$

where *kgw* is the amount of water in kilograms that remains after evaporating a solution that contains 1 kg of water initially. This equation shows that for values of $Kh = P_{satH2O}$, a solute is neither concentrated nor diluted upon water removal by evaporation. For values of $Kh < P_{satH2O}$, the solute concentrates (*cfact* > 1) because the removal of water into the gas phase exceeds the volatilization of the solute. Conversely, for values of $Kh > P_{satH2O}$ (*cfact* < 1), the solute concentration decreases because the volatilization of the solute exceeds that of water.

Kh values for Hg were derived using data for equilibrium constants as a function of temperature for the reaction Hg(v) ↔ Hg(aq) reported by Spycher and Reed (1989). These data were initially derived using Gibbs free energy and solubility data from the literature, and are used for the geochemical and reactive transport simulations discussed later. These data were not corrected for pressure. To evaluate the pressure effect, derived *Kh* values were corrected by applying a Poynting factor. This factor was calculated using an average molar liquid Hg volume (14.8 cm^3/mol) estimated from the molecular weight and density data shown in Table 2-1. This approach is approximate as it does not consider the molar volume change with temperature and pressure, which is considered a second order effect. Original and pressure-corrected *Kh* values for Hg were compared to the values reported by NIST (2011) and Andersson et al. (2008), and to the saturation pressure curve of pure water (Wagner and Pruss, 2002) (Figure 2-3). These data show that *Kh* values for Hg are orders of magnitude larger than the water-vapor saturation pressure. Therefore, aqueous Hg is not expected to concentrate in solution upon removal of water by evaporation into CO_2, thus implying that it would not concentrate near the well.

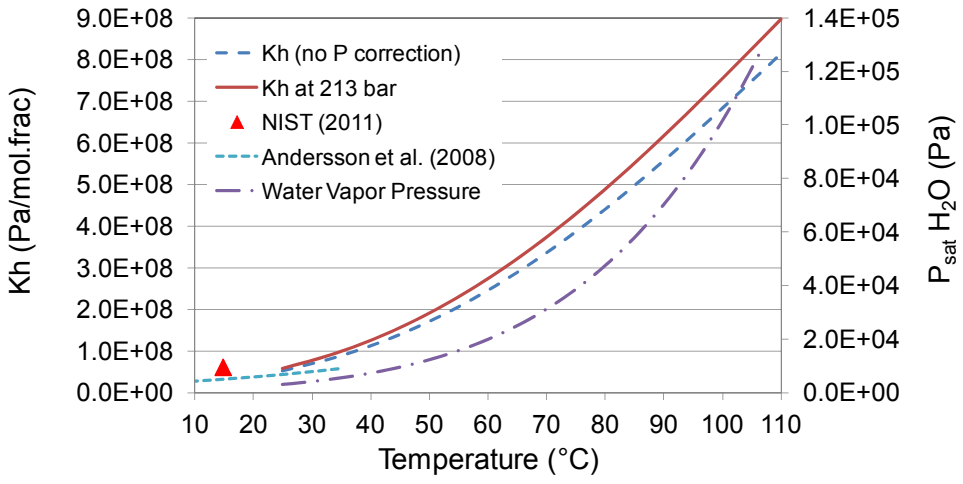

Figure 2-3. *Henry's law constant for Hg (Kh, see text) (left-hand side axis) and water vapor saturation pressure (right-hand side axis) versus temperature.*

As an example, Eq. 2-4 was applied using the *Kh* value for Hg at 106°C (7.6×10^8 Pa) and successively smaller values up to 7.6×10^2 Pa (Figure 2-4). This figure clearly shows that evaporative concentration would only be possible at *Kh* values below 1.25×10^5 Pa, the water vapor saturation pressure at 106°C. This value is more than three orders of magnitude lower than the *Kh* value estimated for Hg at this temperature.

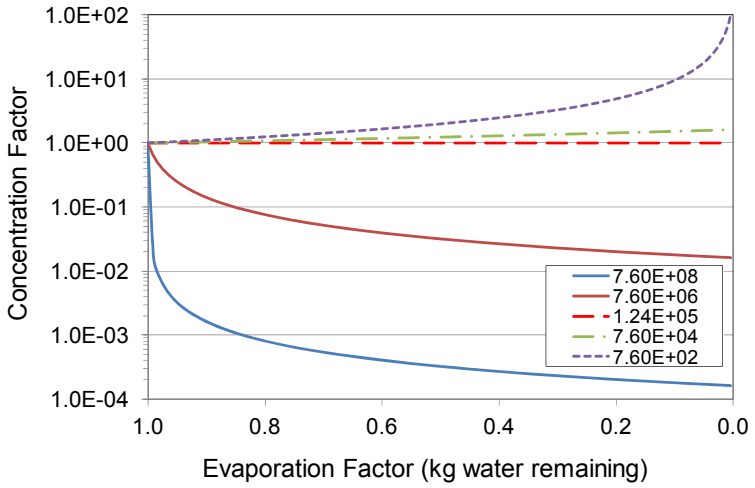

Figure 2-4. *Application of Eq. 2-4 using the Kh value (Pa/mol.frac) estimated for Hg at 106°C and successively smaller values. Concentration factors > 1 indicate evaporative concentration, whereas values < 1 indicate decreasing concentrations of the solute upon evaporation, directly proportional to the value of the concentration factor.*

To further illustrate and verify the behavior of Hg upon evaporative concentration, a simple numerical simulation was set up using TOUGH2/EOS7C (Oldenburg et al., 2004) to simulate the evaporation of different solutions, each containing a dissolved (generic) compound with a different volatility. An example of such solutions is illustrated in Figure 2-5, which shows three beakers containing aqueous mixtures with solutes (NaCl, CH_4, and Hg) of increasing volatility. For example, when H_2O evaporates from the beaker containing the NaCl solution, NaCl concentrates because it does not volatilize. In the case of the middle beaker, CH_4 can be expected to volatilize faster than H_2O resulting in lower concentration of CH_4 in the solution as time goes on. What about the beaker containing dissolved Hg? Does Hg concentrate or diminish as evaporation into a dry CO_2 stream occurs?

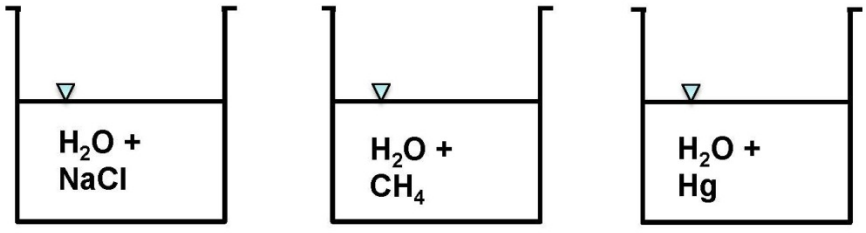

Figure 2-5. *Three hypothetical beakers containing aqueous mixtures of dissolved components with contrasting volatility.*

This question is answered by a numerical experiment that examines the evolution of Hg concentration in the aqueous phase as evaporation of H_2O into a through-flowing CO_2 stream occurs at 213 bars and 106°C. Three grid blocks were defined as shown in Figure 2-6. Dry CO_2 is injected into the first grid block, which is initially filled with a small amount of aqueous phase that quickly dries up. This CO_2 flows directly into the second grid block that contains a two-phase mixture of gas and aqueous phase, where the aqueous phase contains Hg at a concentration of 5.6×10^{-8} by mass fraction. In this second grid block, instantaneous equilibrium concentrations of H_2O, CO_2, and Hg in the gas and aqueous phases are calculated. This gas phase then flows into the third grid block which is an effective sink for whatever phases and components flow into it. The question we have posed can be answered by simply monitoring the aqueous phase concentration in the second grid block; in short, does Hg concentration increase or decrease as dry CO_2 flows through?

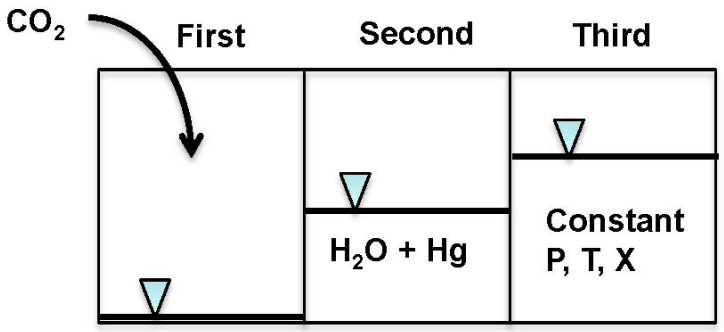

Figure 2-6. *Sketch of the three grid blocks used to model the evolution of Hg concentration in the aqueous phase of the second grid block as dry CO_2 flows through it.*

Simulations were carried out using TOUGH2/EOS7C where we assigned various values to the Henry's Constant of the tracer (component 4) so that we could model the system for Hg as well as hypothetical more- and less-volatile components. Results are shown in Figure 2-7 by curves of gas saturation (left-hand side vertical axis) and Hg concentration (mass fraction in the liquid (aqueous) phase) in the second grid block. As shown, the gas saturation increases steadily as the H_2O component evaporates from the aqueous phase. For Hg, which has $1/Kh = 1.22 \times 10^{-9}$ Pa^{-1} (solid blue curve), the Hg concentration rapidly declines with time, indicating that Hg is more volatile than H_2O. This curve shows the primary result of the numerical experiment which is that Hg will not concentrate in the aqueous phase as dry CO_2 flows through. Additional results for hypothetical solutes with various $1/Kh$ values are shown in Figure 2-7. For $1/Kh$ values larger than 7.994×10^{-6} Pa^{-1}, the solute will concentrate as evaporation occurs. What is this critical value of $1/Kh$ that separates concentrating from non-concentrating solutes subject to contact with dry CO_2? It is the inverse saturation pressure of water at the given P-T conditions. In other words, if a solute is more volatile than water in the CO_2 stream, its concentration will decrease in the aqueous phase as drying occurs. If the solute is less volatile than water, its concentration will increase. This result confirms that the concentration of Hg in a two-phase groundwater-gas region will decrease as dry CO_2 flows through because the Hg component is more volatile than the H_2O component into the CO_2 stream.

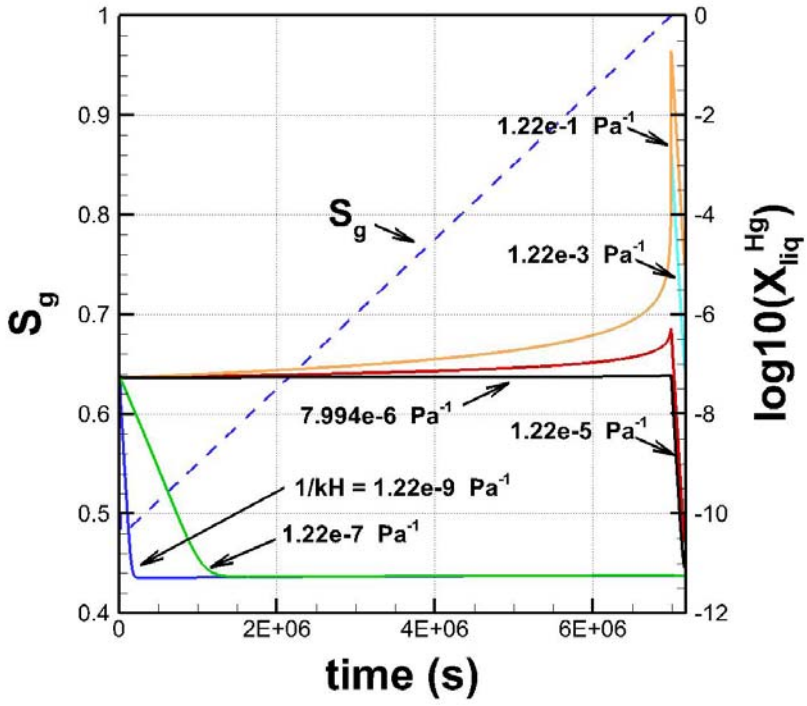

Figure 2-7. *TOUGH2/EOS7C results of gas saturation (S_g) and log mass fraction of Hg in the liquid (aqueous) phase as a function of time in the second grid block for solutes with various 1/Kh values. The curve for Hg is shown by the blue solid line ($1/Kh = 1.22 \times 10^{-9}$ Pa^{-1}).*

3 GEOCHEMICAL MODELING

In the previous sections of this report, simple and approximate analyses were presented to arrive at the conclusion that, for the small Hg gas phase concentrations considered here, any Hg deposition from the gas phase would have to be quite localized (scales of centimeters) to result in non-negligible porosity change (i.e., porosity change that would substantially affect permeability). These calculations also indicate that the condensation of Hg as liquid mercury would be highly unlikely. Although insightful, these preliminary analyses do not consider water-sediment chemical interactions, their effect on the speciation of Hg and its aqueous concentration, or the thermodynamic tendency for precipitation of cinnabar (HgS(s)) preferentially over the stability of Hg(l) in the presence of sulfide which occurs naturally in formation brines in addition to being an impurity in CO_2. For this reason, we present below results of geochemical simulations considering the chemical reaction between formation water, sediments, and a CO_2+Hg mixture. These simulations were performed using the CHILLER numerical model (Reed, 1982, 1998), and do not consider transport. These serve as a basis for the development of more complex reactive transport simulations using TOUGHREACT (Xu et al., 2011) presented later in this report.

All geochemical and reactive transport discussed in this report rely on an external set of thermodynamic data which are discussed in Section 3.1. The mineralogy of the reservoir formation considered is discussed in Section 3.2. A formation water composition is also necessary to run geochemical and reactive transport simulations. Because such waters are typically affected by degassing and mineral precipitation when they are sampled (e.g., Palandri and Reed, 2001), the composition of the deep (in-situ) brine needs to be reconstructed. Of most importance for these numerical simulations is the reconciliation of measured water compositions and observed mineralogy into a consistent dataset that yields chemically steady initial conditions for a particular geochemical system. This was done here as discussed in Section 3.3. The results of the CHILLER simulations are presented in Section 3.4. Reactive transport simulations are discussed in Section 4.

3.1 Thermodynamic Data

In this study, the thermodynamic database compiled by Reed and Palandri (2006) (*soltherm.h06*) was selected. This database has been developed and refined over decades, and applied to the geochemical investigation of many different water-rock systems over a wide range of temperatures (up to 350°C, along the saturation pressure curve of water). This database relies on Gibbs free energy data primarily from Holland and Powell (1998) for minerals, and primarily from SUPCRT92 (Johnson et al., 1992) for aqueous species. Spycher and Reed (1989) compiled thermodynamic data for Hg aqueous, solid, and gas species to study the behavior of volatile metals in hydrothermal systems. These Hg data are part of the *soltherm.h06* database, and are used here without further modifications. Equilibrium constants for a few minerals were either updated, or newly added from recent sources. These include data from Bénézeth et al. (2007) for dawsonite, Arnorsson and Stefansson (1999) for feldspars (adjusted for consistency with the aqueous silica data in the database), and Yang and Steefel (2008) for kaolinite. Equilibrium constants for Fe-rich chlorite were computed by assuming an ideal solution of 70 mol% clinochlore and 30 mol% daphnite, using the equilibrium constants derived from the data of Holland and Powell (1998) for these end members. Glauconite was also added to the database using the composition and equilibrium constant at 25°C reported by Tardy and Fritz (1981), and

extrapolated to higher temperature following the trend of the muscovite equilibrium constants given in the database (computed with the data of Holland and Powell, 1998).

3.2 Mineralogy of the Reservoir Formation

The reservoir mineralogy used in the simulations was chosen to represent a typical marine sandstone/siltstone with minor claystone, including silica and carbonates as common cements, glauconite as a common accessory mineral, some illite/mica, and disseminated pyrite throughout. Specific mineral abundances were defined on the basis of data provided by the site operator as well as from the literature, as shown in Table 3-1. Other secondary minerals allowed to form during the simulations include siderite, kaolinite, dawsonite, illite, albite, magnesite, and chalcedony.

Table 3-1. *Mineralogical composition of the deep marine sandstone formation assumed for the simulations. Other minerals are allowed to form in the simulations (see text).*

Minerals	Estimated Wt %	Vol %
Calcite	0.5	0.49
Dolomite	0.5	0.46
Ankerite	0.5	0.41
Glauconite	7	6.95
Fe-chlorite	2	2.02
Quartz	75	75.36
Pyrite	0.5	0.3
K-spar	8	8.3
Plagioclase (An10)	1	1.01
Muscovite	5	4.7

3.3 Reconstruction of the Formation Water

The composition of the deep formation water was determined on the basis of water analyses provided by the site operator (Table 3-2, 2nd column from left). The concentrations of some parameters that were either not reported, or likely to have been affected by re-equilibration upon sampling/flashing, were recomputed. The reconstruction of the deep water composition was carried out using GeoT (Spycher et al, 2013, 2014), a geochemical speciation code recently developed to reconstitute the composition of deep geothermal waters, and to evaluate their temperature at depth based on the saturation indices of reservoir minerals (following Reed and Spycher, 1984). In a first stage, the concentrations of Ca, Mg, Si, Al, and total sufide (as HS^-) were computed and/or manually adjusted to yield equilibration of the water with, respectively, calcite, dolomite, quartz, kaolinite, and pyrite at the formation temperature of 106°C. Simultaneously, the deep (in-situ) pH was recomputed by electrical charge balance constraint. Because deep formation waters are known to contain organic acids (e.g., Palandri and Reed, 2001), acetate was also added to the water by an amount that yielded the best clustering of saturation indices near zero (the equilibrium point) at the formation temperature for the reservoir

minerals considered (Figure 3-1). The water composition obtained in this way was then equilibrated using CHILLER to fractionate any remaining minerals computed to form at 106°C. The resulting water composition (Table 3-2, 3rd column from left) was used as the initial composition for the CHILLER simulations discussed below.

A chemically steady or nearly steady initial water composition (upon reaction with formation minerals) is a prerequisite for reliable simulations of reactive transport, and is typically difficult to achieve. For the TOUGHREACT simulations presented later (Section 4), the reconstructed water was further reacted under kinetic constraints with the minerals shown in Table 3-1, for 1000 years, a point at which essentially steady conditions were achieved. The composition obtained in this way (Table 3-2, right column) is further discussed in Section 4.2.

The computed concentrations of most components in the reconstructed and reacted waters (Table 3-2) do not depart significantly from their original values. This, along with the fact that these computed compositions yield an equilibrium mineral assemblage consistent with field data, provides reasonable confidence in the reconstruction approach, the selected mineral assemblage, and the thermodynamic data used in the simulations. It should be noted, however, that the recomputed total dissolved concentrations of Fe and sulfate (as SO_4) are significantly lower than measured values. It is likely that the measured Fe concentration does not reflect true dissolved Fe, which is common with Fe analyses, and/or possibly that it reflects contamination from engineered components. For SO_4, calculated concentrations below measured values reflect a chemical reduction to sulfide during the computations, which is most pronounced in the reacted water after 1000 years (Table 3-2). This suggests that the measured SO_4 concentration could represent sulfide that was oxidized upon sampling, and/or that redox equilibrium is not fully achieved in this system. Further discussions of the reacted water composition used for reactive transport (Table 3-2, right column) are presented in Section 4.2.

Table 3-2. *Composition of the formation water considered in this study (in ppm). The "Reconstructed" and "Reacted" columns show, respectively, computed initial compositions used for geochemical modeling with CHILLER, and reactive transport modeling with TOUGHREACT.*

Constituent	Measured	Reconstructed	Reacted 1000 years
pH (25°C)	8.47		
pH (106°C)		6.9	7.1
Cl	2185	2208	2209
SO_4	31	3.6	0.033
HCO_3 *	2167	2331	3114
H_2S **	--	0.15	0.52
Si	--	25	45
Al	--	1.4E-03	2.1E-03
Ca	13.1	6.1	2.7
Mg	3.1	1.6	0.71
Fe	6.86	1.70E-03	7.1E-04
K	449	549	59
Na	2250	2266	2874
Acetate	--	1181	1181
log(fO_2)	--	-53	-54

*Total dissolved inorganic carbon as HCO_3; **total dissolved sulfide as H_2S.

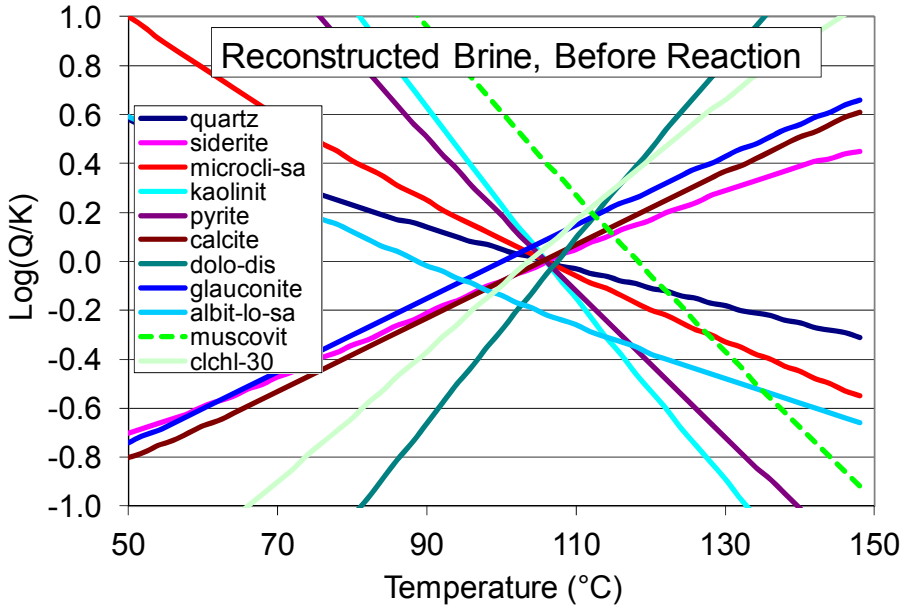

Figure 3-1. *Computed saturation indices (log(Q/K)) of various minerals using the reconstructed formation water composition shown in Table 3-2. Most of the formation minerals considered in this study (Table 3-1) cluster near zero (the equilibrium point) at the formation temperature of 106°C (clchl-30 stands for Fe-chlorite).*

3.4 Chemical Interaction between Hg-Bearing CO_2, Formation Water, and Sediments

Here we describe simulations run using CHILLER that neglect transport as a prelude to full reactive transport simulations (Section 4). The modeling consisted of first reacting (numerically "titrating") CO_2 into the formation water (Table 3-2) until the development of a separate CO_2 phase (~40% by volume) at a system pressure of about 200 bar. Mercury was included into the titrated CO_2 at a concentration of 190 ppmV. In a second stage, the sediment mineralogy (Table 3-1) was reacted (in small, finite increments) with the brine-CO_2+Hg assemblage, until a water/sediment ratio ~1, a point at which little further reaction took place (Figure 3-2).

With this type of "titration" approach, minerals reaching (or already at) equilibrium with the solution are not further titrated at each reaction step, thus approximating dissolution of the sediment in finite amounts until thermodynamic equilibrium. At each reaction step, any mineral that becomes thermodynamically stable is allowed to precipitate. The mineral selection is made automatically from the large list (>200) of minerals in the input thermodynamic database. However, minerals that are not deemed to belong in the geochemical system can be suppressed (on grounds of slow precipitation kinetics at low temperatures, such as for metamorphic minerals), enabling the next most thermodynamically favored mineral to form. In the present case, for example, quartz (SiO_2) is not allowed to form because its precipitation at temperatures below about 200°C is quite slow, and chalcedony is preferred as the precipitating SiO_2 phase (Figure 3-2c). This type of modeling is quite useful to determine alteration products from all kinds of water-gas-rock interactions on both thermodynamic and kinetic grounds. It is also useful by this approach to examine Hg speciation, and reaction products (i.e., secondary minerals) that can then be considered for reactive transport simulations under full kinetic constraints.

The pH of the formation water is lowered by the carbonic acid released by the dissolution of CO_2. The pH initially drops down to about 4.7 (without sediments added in the system), then becomes buffered near 5.2 when sediments are titrated into the system (Figures 3-2b,c). The main reaction products are chalcedony forming from feldspar and quartz dissolution, and siderite from primarily Fe-chlorite dissolution. Kaolinite initially forms at the expense of plagioclase dissolution but is replaced by muscovite as the pH increases. The dissolution of calcite and chlorite yields enough Mg and Ca in solution for the precipitation of magnesite and ankerite to take place after a certain amount of sediment has been reacted (about 40 g per initial kilogram of water, Figure 3-2c). The volume balance between dissolving (Table 3-1) and precipitating (Figure 3-2c) minerals yields an unnoticeable porosity change (Figure 3-2b).

Cinnabar (HgS(s)) is found to be thermodynamically stable as soon as the Hg-bearing CO_2 reacts with the formation water, which contains small amounts of dissolved sulfide. The precipitation of cinnabar is then predicted to continue upon reaction with the sediments (Figure 3-2c). Liquid mercury (Hg(l)) is not found to be thermodynamically stable at any point during the simulation, with a saturation index remaining near -2.5. As shown by the reaction and equilibrium constants below, the formation of cinnabar is strongly favored, thermodynamically, relative to Hg(l) when sulfide is present:

$$HgS(s) + H_2O = Hg(l) + 0.25\ SO_4^{-2} + 0.75\ H_2S(aq) + 0.5\ H^+$$
$$\log(K) = -13.30\ (25°C)\ \text{and}\ -10.42\ (100°C) \qquad (3\text{-}1)$$

This reaction also shows that low pH (high H^+) would further favor the precipitation of cinnabar relative to liquid mercury.

The dissolved Hg concentration is very small (on the order of 10^{-8} molal, or ~2 ppb) (Figure 3-2a). Aqueous Hg is computed to consist entirely of the dissolved Hg^0 species. It will be shown later (Section 4.3) that at higher sulfide concentrations, caused by including H_2S as an impurity in CO_2, Hg-S aqueous species can become dominant and raise the Hg solubility by a factor about 2 under the present conditions, which is still quite low.

It should be noted that the simulated total dissolved Hg and sulfide (shown as HS^-) concentrations in Figure 3-2a, as well as pyrite amounts in Figure 3-2c, display a dense sawtooth pattern. This is an artifact from stopping the titration (reaction) of a mineral (in this case pyrite) once this mineral reaches equilibrium with the solution. Under the condition of low pH and low sulfide concentration here, cinnabar forms preferentially relative to pyrite, consistent with the reaction:

$$HgS(s) + Fe^{+2} + H_2S(aq) = FeS_2(s) + Hg(aq) + 2H^+$$
$$\log(K) = -7.40\ (25°C) \text{ and } -6.19\ (100°C) \qquad (3\text{-}2)$$

The precipitation of cinnabar (HgS) thus competes with pyrite (FeS_2), which is not replenished by the reacting sediment until it becomes fully depleted (below saturation). This behavior yields alternating cycles of complete pyrite dissolution followed by reprecipitation, which cannot be avoided with this type of simulation (except at extremely small prescribed reaction increments in this case, which create very long and impractical simulation times).

The results of these simulations are consistent with the preliminary calculations presented earlier in that the precipitation of liquid mercury from the CO_2 phase (i.e., Hg(l) condensation) is not expected in this system. However, the presence of even a very small amount of dissolved sulfide in the formation water causes cinnabar precipitation. This mineral has a very low solubility, and therefore the predicted dissolved Hg concentrations in the formation water are very low (ppb range). Essentially all the Hg initially in the CO_2 is expected to precipitate in the formation as cinnabar. As discussed in Section 2.2 (Figure 2-1), the effect of cinnabar precipitation on porosity (and thus permeability) would depend on the scale over which such precipitation takes place. The spatial aspect of cinnabar precipitation, however, cannot be investigated using “batch” reaction simulations such as those presented above. To address this question, a full reactive transport model was developed, as described in the following sections.

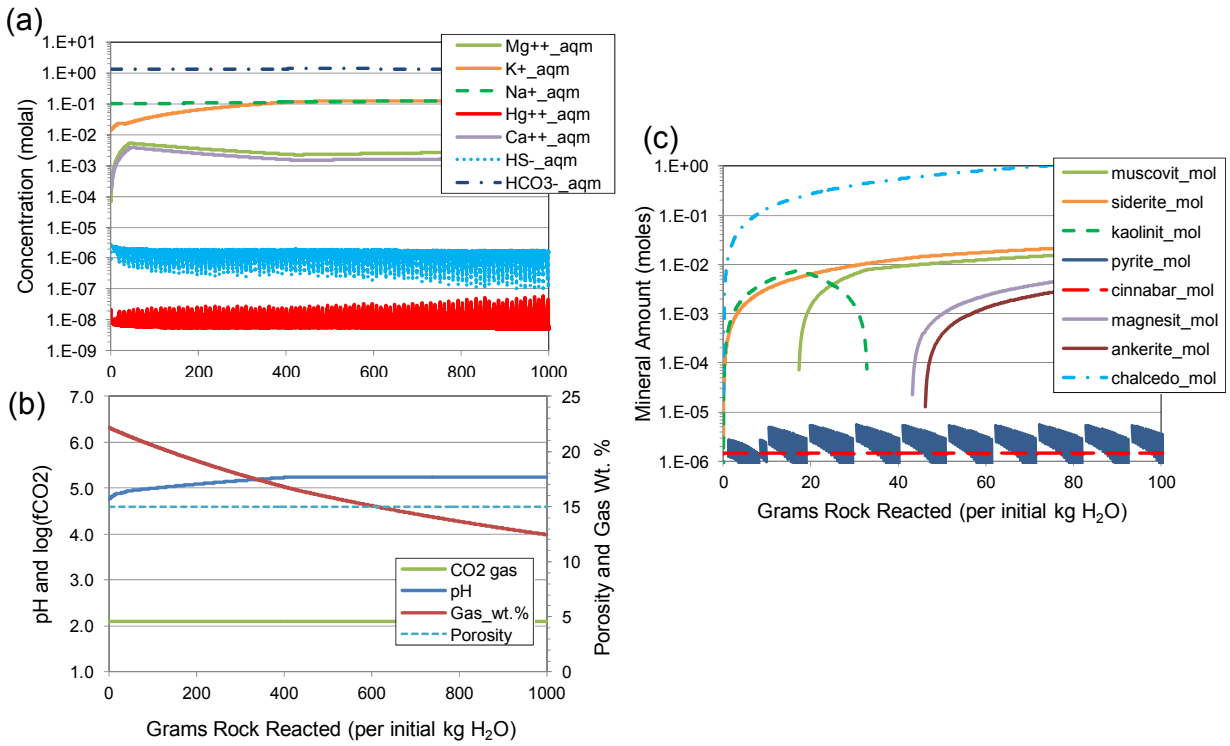

Figure 3-2. *Simulated reaction of sediments ("rock"), formation water, and Hg-bearing CO_2 at 106°C and 213 bar. (a) Total dissolved concentrations of major aqueous species, sulfide and Hg. (b) CO_2 gas amount (Gas_wt.%) and fugacity (CO_2 gas), pH, and porosity. (c) Precipitating minerals (shown only for the first 100 grams of reaction increment, for detail; these trends remain steady with further reaction). See text for discussion.*

4 REACTIVE TRANSPORT MODELING

The injection of Hg- and H_2S-bearing CO_2 into a deep sandstone formation was simulated using a reactive transport model to investigate the coupled hydrological and geochemical processes taking place within the target formation around the injection well. Particular interest was given to the spatial distribution of Hg deposition and the porosity change around the injection well. Initially, simulations were carried out using TOUGHREACT V2 (Xu et al., 2011) coupled with ECO2N (Pruess and Spycher, 2007) and modified to allow for the transport of multiple trace gases with the CO_2. These preliminary simulations were run on a rather coarse numerical grid and had to make use of boundary conditions difficult to set up to simulate the injection of trace gases with the CO_2. Subsequent simulations were run on a much finer numerical grid and using a newly developed parallel version of TOUGHREACT OMP-V2.3g (Sonnenthal et al., 2014). In synergy with other ongoing projects, this code version was modified to allow injection of multiple trace gases of given concentrations within a main "carrier" gas (in this case CO_2). The setup of these simulations (Sections 4.1 and 4.2) and model results (Section 4.3) are discussed below.

4.1 Model Setup and Input Parameters

4.1.1 Hydrological Setup and Parameters

The model was set up as a two-dimensional (2D) vertical *X*-*Z* radial numerical mesh, as shown on Figures 4-1 and 4-2. CO_2 injection is taking place within a 300 m-long open borehole (radius 0.08 m) centered on a target formation with a total thickness of 400 m. The numerical mesh comprises 9700 grid blocks, including 100 horizontal layers, each of a constant 4 m thickness, with increasing grid spacing in the horizontal direction starting at a well radius of 0.08 m, then increasing progressively away from the well (Figure 4-2).

Final simulations discussed below were run using a maximum time step of 6 hours. This time-step value was found to remain below the Courant limit computed for aqueous-phase flow in all model grid blocks and at all times. However, because of the high CO_2 injection rate and fine space discretization near the well, this value was found to exceed the Courant limit for gas-phase flow (~ 2 minutes at the well) for up to a distance of about 2 to 3 m from the injection well. Nevertheless, test simulations at time steps below the Courant limit for the gas phase over limited simulated time periods indicated that a maximum time step of 6 hours should provide a reasonable compromise between computing efficiency and numerical accuracy.

For simplicity, hydrological properties were assumed homogenous throughout (Table 4-1), and model boundaries were closed, with the lateral boundary located far away from the injection well (10 km). Tests using a fixed-pressure lateral boundary showed somewhat more lateral spreading of the CO_2 plume than with a closed boundary (~ 2100 m versus ~ 2500 m after 40 years of injection), but otherwise similar results.

It should be noted that hydrodynamic dispersion is not explicitly modeled in these simulations. Results are subject to numerical dispersion, however, which can be viewed as some "proxy" for hydrodynamic dispersion. Numerical dispersivity values are approximately given by the model grid-block sizes ($\Delta x/2$ in the *X* direction and $\Delta z/2$ in the *Z* direction).

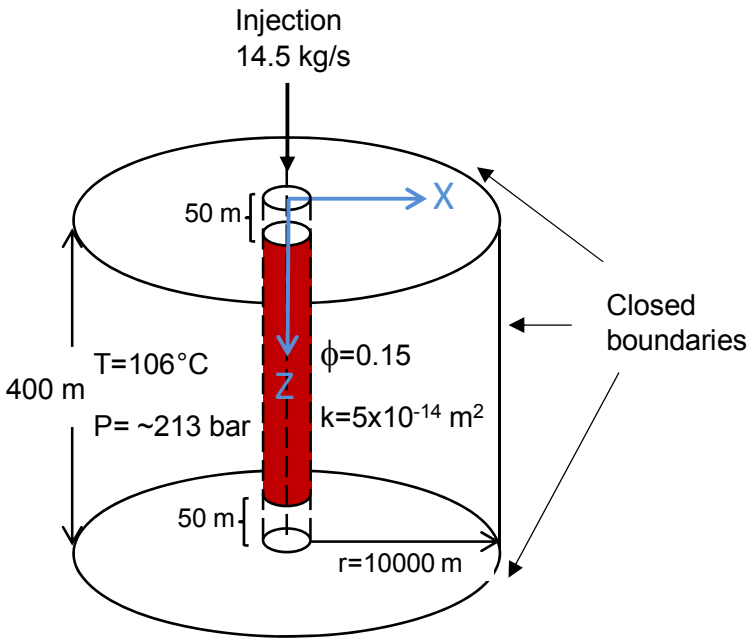

Figure 4-1. *Schematic representation of the reactive transport model setup (not to scale). The injection interval (300 m) is shown in red (not to scale).*

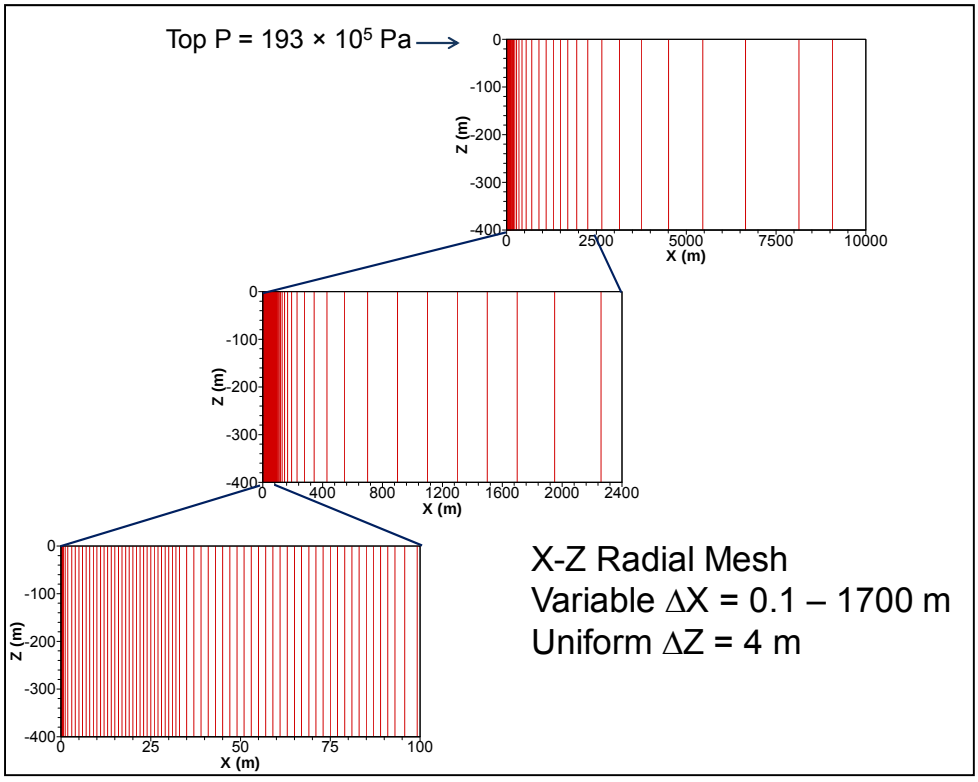

Figure 4-2. *Radial discretization of the numerical domain with 100 uniform-thickness vertical layers not shown. The center of the injection well is located at X = 0.*

Table 4-1. *Hydrological properties of the reactive transport model.*

Property	Value
Porosity (ϕ)	0.15
Dip	0 degrees
Pressure at top of domain (initial) Pressure at bottom of domain (initial)	1.93×10^7 Pa 2.33×10^7 Pa
Temperature (isothermal)	106°C
Permeability (k)	5.0×10^{-14} m^2
Pore compressibility	10^{-10} Pa^{-1}
Capillary Pressure (P_{cap}) and Relative Permeability (k_r) *Terminology:* $\lambda = m = 1\text{-}1/n$ = power in expressions for P_{cap} S_{lr} = aqueous-phase residual saturation S_{gr}= gas-phase residual saturation $P_{c0} = \alpha^{-1}$ = capillary pressure strength between aqueous and gas phase P_{cmax} = maximum possible value of P_{cap}	van Genuchten[a] capillary pressure and relative permeability for liquid, Corey[a] relative permeability for gas $\lambda = 0.40$ $S_{lr} = 0.27$ $S_{gr} = 0.01$ $P_{c0} = 1190$ Pa $P_{cmax} = 1 \times 10^8$ Pa
Well injection rate	14.5 kg/s

[a] See Pruess et al. (1999 and 2011).

4.1.2 Reactive Processes and Main Assumptions

In addition to multiphase flow and transport of aqueous and gaseous species, the simulations considered reactions between these species and minerals. Most minerals were assumed to react under kinetic constraints, as discussed below. Potentially forming Hg phases (cinnabar and liquid mercury) were assumed to precipitate under (local) equilibrium constraints which represent the equivalent of very fast rates of reaction. In doing so, the amount of Hg deposition was overestimated rather than underestimated. Kinetic data for these Hg phases were not readily available, and thus equilibrium was deemed to be a conservative case for looking at potential permeability changes from Hg precipitation.

Reactions between aqueous species, including redox reactions, and between the formation water and gaseous species (CO_2, Hg, and H_2S) were assumed to proceed under (local) thermodynamic equilibrium. Except for redox species, these reactions are typically fast, such that the assumption of local equilibrium is reasonable. However, redox reactions can be quite slow at low temperatures. In the present case at 106°C, it is possible that redox equilibrium is not fully reached. Because the precipitation of cinnabar ($Hg^{(+2)}S^{(-2)}$) from zero-valent Hg in the gas phase represents the oxidation of Hg with concomitant sulfate ($S^{(+6)}O^{(-2)}_4$) reduction to sulfide ($H^{(+)}_2S^{(-2)}$) (following a reaction with the same stoichiometry as reaction 3-1), simulating this reaction assuming equilibrium can be deemed conservative in terms of maximizing the amount of cinnabar precipitation. In terms of maximizing the precipitation (condensation) of Hg(l), this assumption would not be conservative, however, because slow cinnabar precipitation would increase the potential for Hg(l) deposition. However, it was shown earlier (Sections 2.3 and (Section 3.4) that the concentration of Hg in the CO_2 phase is much smaller than the

concentration required for Hg(l) to condense, thus slowing down the precipitation of cinnabar would have no effect on the condensation of Hg(l).

For all simulations, the effect of mineral precipitation and dissolution was coupled to porosity assuming uniform coating of pore spaces, and using volumetric data for minerals from the literature to compute volume changes upon dissolution or precipitation. Porosity was coupled to permeability using the Kozeny-Carman relationship, and to capillary pressure through Leverett scaling. However, results discussed below show that the computed porosity change was too small to cause significant permeability change for the injection cases investigated.

The partitioning of Hg in the gas phase was computed assuming ideal-gas behavior, thus assuming equality of partial pressure and fugacity. Also, the effect of pressure on the thermodynamic constant expressing equilibrium between aqueous Hg (Hg^0(aq)) and gaseous Hg (Hg^0(g)) was neglected. It is shown later (Section 5) that these assumptions are likely to result in overestimated amounts of Hg deposition, and thus are deemed conservative.

4.1.3 Geochemical Parameters

Mineralogical Data and Initial Water Composition

The same initial mineralogical composition was assumed as for the geochemical simulations presented earlier (Table 3-1). In addition, the following secondary phases were allowed to form (as products of water-CO_2-sediment chemical interactions): kaolinite, illite, magnesite, siderite, and dawsonite. This list of potentially forming phases was established on the basis of the geochemical modeling results (Section 3.4) as well as typical alteration products of CO_2-sediment interactions reported in published experimental and modeling studies. Cinnabar and liquid mercury were also added to this list as potential Hg-precipitating phases.

The composition of the formation water was discussed in Section 3.3. The initial composition used for injection simulations is shown in the last column of Table 3-2, and further discussed below (Section 4.2).

Thermodynamic and Kinetic Data

The same thermodynamic data were used as for the geochemical simulations (Section 3.1). In contrast with these simulations, the precipitation and dissolution of most minerals were modeled to proceed under kinetic constraints. A general rate law derived from transition state theory (Lasaga et al., 1994) was used for mineral dissolution and precipitation:

$$R_m = \pm A_m k_m (\Omega_m^n - 1)^p \tag{4-1}$$

where k is the rate constant (moles per unit mineral surface area and unit time), A_m is the specific reactive surface area per kg H_2O, Ω_m is the kinetic mineral saturation ratio (Q/K), and exponents n and p are either determined from experiments or taken equal to one. The value of the kinetic rate constant (k) can vary with the activity of other species, such as with pH (Lasaga et al., 1994; Palandri and Kharaka, 2004) as follows:

$$k = k_{25}^{nu} \exp\left[\frac{-E_a^{nu}}{R}\left(\frac{1}{T} - \frac{1}{298.15}\right)\right] + k_{25}^{H} \exp\left[\frac{-E_a^{H}}{R}\left(\frac{1}{T} - \frac{1}{298.15}\right)\right] a_{H^+}^{n_H} + k_{25}^{OH} \exp\left[\frac{-E_a^{OH}}{R}\left(\frac{1}{T} - \frac{1}{298.15}\right)\right] a_{H^+}^{n_{OH}} \quad (4\text{-}2)$$

where superscripts or subscripts *nu*, *H*, and *OH* indicate neutral, acid and base mechanisms, respectively; *a* is the activity of the species (in this case H^+); n_H and n_{OH} are power terms (constant); and E_a is the activation energy for each mechanism.

These kinetic rate parameters were taken primarily from the compilation of Palandri and Kharaka (2004) and updated with data from Yang and Steefel (2008) for kaolinite, Hellevang et al. (2010) for dawsonite, Golubev et al. (2009) and Duckworth and Martin (2004) for siderite (and applying the same data to ankerite), and Alekseyef (2007) and Brandt et al. (2003) for chlorite (Table 4-2). Glauconite was given the same parameters as muscovite. Rates were assumed reversible, except for quartz which was only allowed to dissolve. Chalcedony was included as a potential silica precipitation phase, using the rate law and data of Carrol et al. (1998) for amorphous silica.

Input-specific surface areas used in the computation of A_m in Eq. 4-1 were calculated assuming spherical grain sizes of about 0.2 mm, yielding input surface areas of 3×10^4 m^2/m^3 (on the order of ~10 cm^2/g, depending on density). It should be noted that the uncertainty in A_m is typically quite large, and can be up to several orders of magnitude.

Table 4-2. *Kinetic parameters for equation 4-2, with k values in mol m^{-2} s^{-1} and Ea values in kJ mol^{-1}. See text for data sources.*

Mineral	$\log(k_H)$ (acid)	Ea_H (acid)	n_H	$\log k_{nu}$ (neut.)	Ea_{nu} (neut.)	$\log(k_{OH})$ (base)	Ea_{OH} (base)	n_{OH} (base)	$\log(k_{CO3})$ (carb.)	Ea_{CO3} (carb)	n_{CO3}
Quartz				-13.34	90.1						
K-feldspar	-10.06	51.7	0.5	-12.41	38	-21.2	94.1	-0.823			
Calcite	-0.3	14.4	1	-5.81	23.5				-3.48	35.4	1
Dolomite	-3.19	36.1	0.5	-7.53	52.2				-5.11	34.8	0.5
Pyrite	-7.52	56.9	-0.5 n_{Fe+3} 0.5	-4.55	56.9						
Kaolinite*	-11.10	65.9	0.777		-12.97	-16.84	17.9	-0.472			
Muscovite	-11.85	22	0.37	-13.55	22	-14.55	22	-0.22			
Glauconite	-11.85	22	0.37	-13.55	22	-14.55	22	-0.22			
Magnesite	-6.38	14.4	1	-9.34	23.5	-5.22	62.8	1			
Siderite	-3.75	48	0.75	-8.65	48						
Dawsonite	-4.48	49.43	0.982	-8.66	63.82						

* Re-fitted data; use with n = 0.333 in Eq. 4-2.

4.2 Initial Hydrologic and Geochemical Conditions

The temperature was assumed to remain constant throughout the simulations, and thermal effects from CO_2 injection were neglected as these are considered second-order effects. Initial hydrostatic pressure conditions were established throughout the model domain prior to running injection simulations, with a pressure of ~213 bar (21.3 MPa) at the middle of the injection interval.

Initial chemical conditions for injection simulations were obtained by running the reactive transport model without injection for about 1000 years, starting with the formation water composition reconstructed as described in Section 3.3. The composition obtained after 1000 years of reaction (Table 3-2, "Reacted" column) is similar to the reconstructed water composition (Table 3-2, "Reconstructed" column) and nearly steady, providing confidence in the coherence of input geochemical data. The decrease in K and Fe concentrations compared to the initially reconstructed water occurs due to some minor precipitation primarily of muscovite and Fe-chlorite. The modeled concentration of SO_4 is found to decrease significantly after reaction, compared to the input value, because of reduction to sulfide. As discussed earlier in Section 3.3, it is possible that measured SO_4 concentrations represent sulfide that oxidized upon sampling. It is also likely that redox equilibrium may not be completely reached in the natural system at 106°C.

4.3 Reactive Transport Model Results

The model was run for a total injection period of 40 years. Three main simulations were run:

- Injection of CO_2 with 200 ppmV H_2S and 190 ppbV Hg (~1.6 mg/std.m^3_{CO2}) (base case)
- Injection of CO_2 with no H_2S and 190 ppbV Hg
- Injection of CO_2 with 200 ppmV H_2S and 7 ppbV Hg (~0.058 mg/std.m^3_{CO2}) (low Hg case)

These simulations yield results qualitatively similar to the geochemical simulations presented earlier, in that Hg is predicted to readily precipitate from the CO_2 as cinnabar, and that porosity in not affected significantly by mineral precipitation and dissolution. The results of these simulations are discussed in detail below. Note that a positive total solid volume fraction change implies a negative porosity change, and vice versa (i.e., total solid volume fraction + porosity = 1).

As shown in Figure 4-3, top, after 40 years, supercritical CO_2 is predicted to migrate to about 2100 m from the injection well, spreading away from the well mostly by buoyancy and accumulation below the top impermeable model boundary. The single-phase CO_2 zone remains within about 60 m of the injection well (Figure 4-3, and blown-up Figure 4-4).

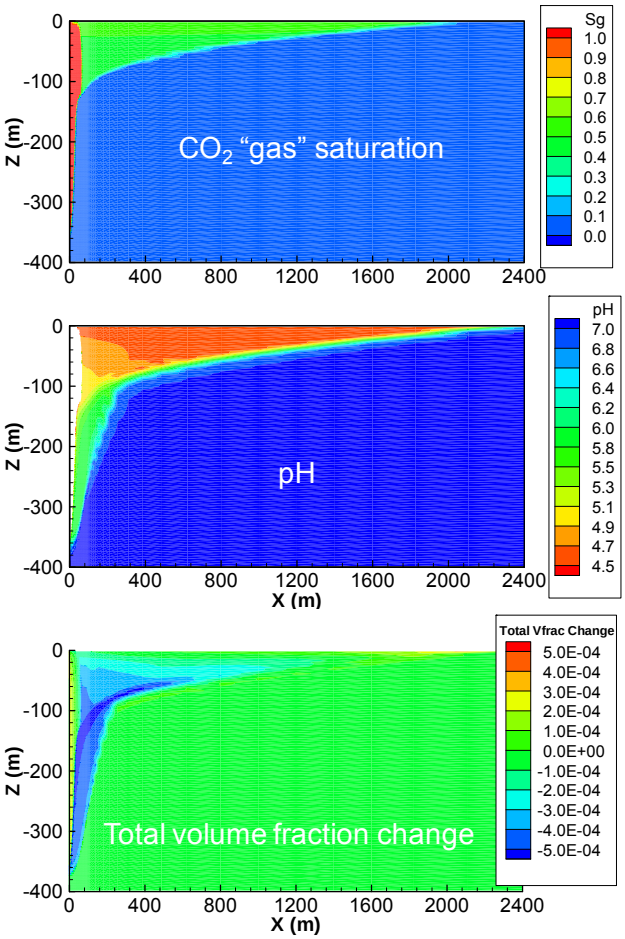

Figure 4-3. *Simulated CO_2 phase (physical) saturation, aqueous phase pH (with the zone of single-phase CO_2 shown as white), and mineral volume fraction change after 40 years of injection. "Total (solid) volume fraction change" corresponds to the opposite of the absolute change in porosity.*

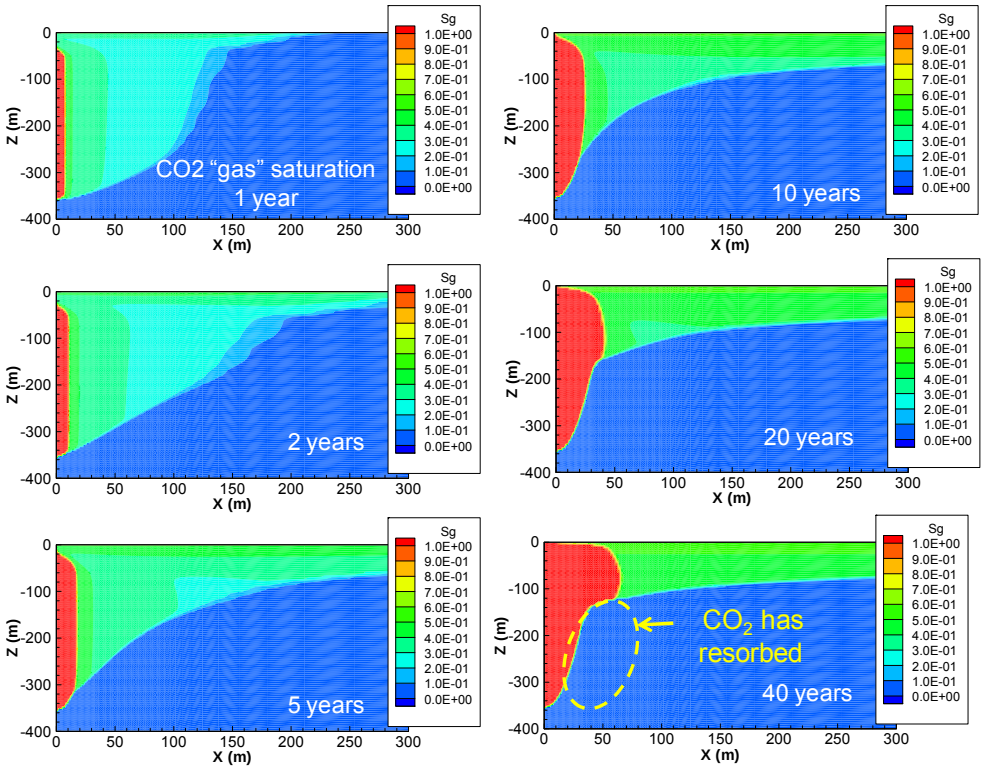

Figure 4-4. *Simulated evolution of the CO_2 plume during 40 years of injection, within 300 m from the injection well. Dashed boundary at 40 years show zone where the CO_2 residual saturation has dissolved away.*

Carbonic acid from the dissolution of CO_2 into the formation water causes a zone of low pH (~4.5–5) that follows the shape of the CO_2 plume (Figure 4-3, middle, and blown-up Figure 4-5). A zone of intermediate pH (~5–6) develops at the fringe of the CO_2 plume. This zone is very thin along the upper edge of the CO_2 plume, but wide and most noticeable within about 300 m around the lower two thirds of the injection well. This region is initially invaded by CO_2 and remains a two-phase zone for close to 10 years (Figure 4-4). After that time, the CO_2 in this region is driven away by buoyancy, and its residual saturation (1%) fully resorbs by dissolution, leaving behind a single-phase water region of intermediate pH that is wider than at other locations along the edge of the CO_2 plume (Figure 4-4). This region coincides with a zone of maximum porosity increase (by about 0.05%, absolute change, i.e. increasing from 0.15 to 0.1505) from mineral dissolution (Figure 4-3, bottom, and blown-up Figure 4-5).

The cases of injection without and with H_2S (at 200 ppmV) in the CO_2 phase show essentially no differences in the distribution of pH (Figure 4-5). A very narrow band of porosity decrease (by about 0.05%, absolute change) is predicted in the case without H_2S at the edge of the single-phase zone, but is not visible in the case with H_2S (Figure 4-5). This porosity decrease is attributed to the replacement of pyrite (FeS_2) by ankerite ($CaFe(CO_3)_2$ when H_2S is deficient (Figure 4-6). Except for this difference, both cases show essentially the same trends and amounts of porosity change (Figure 4-5): a slight porosity increase ahead of the single-phase CO_2 plume (~ 0.05 %, absolute) from mineral dissolution driven by the pH decrease, and a slight decrease

within the single-phase CO_2 plume (also ~ ± 0.05 %, absolute) from mineral precipitation driven in part by water evaporation into the supercritical CO_2. Note that the presence of cinnabar within this zone is not caused by evaporative concentration (see Section 2.4) but from continuous precipitation at the (moving) plume front.

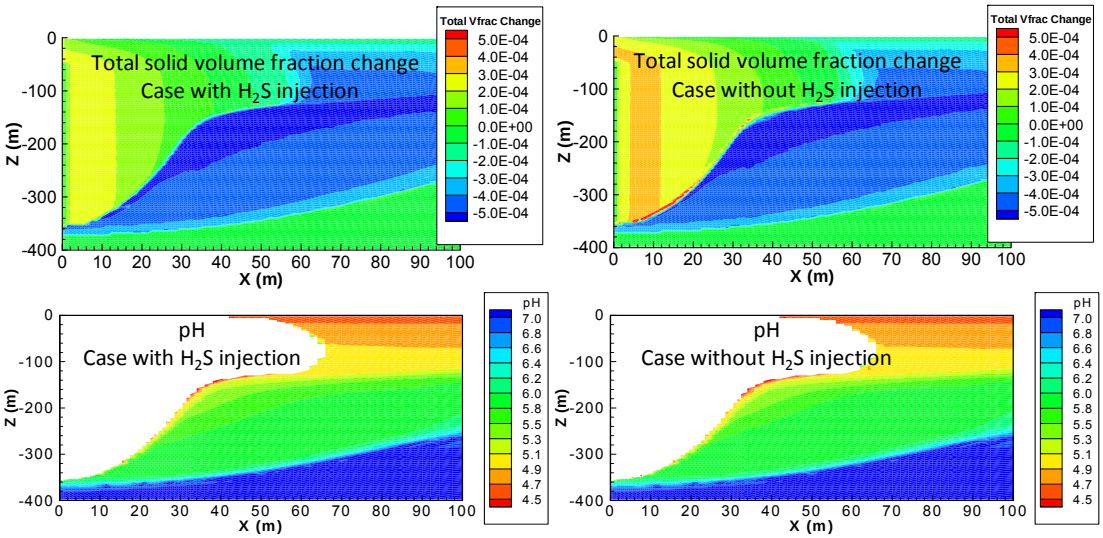

Figure 4-5. *Simulated total volume fraction change of minerals (top), and pH (bottom) after 40 years of CO_2 injection within 100 m of the injection well. The area blanked out (white color) on the pH plots corresponds to the zone of single-phase CO_2 (no water present). "Total solid volume fraction change" corresponds directly to the opposite of the absolute change in porosity.*

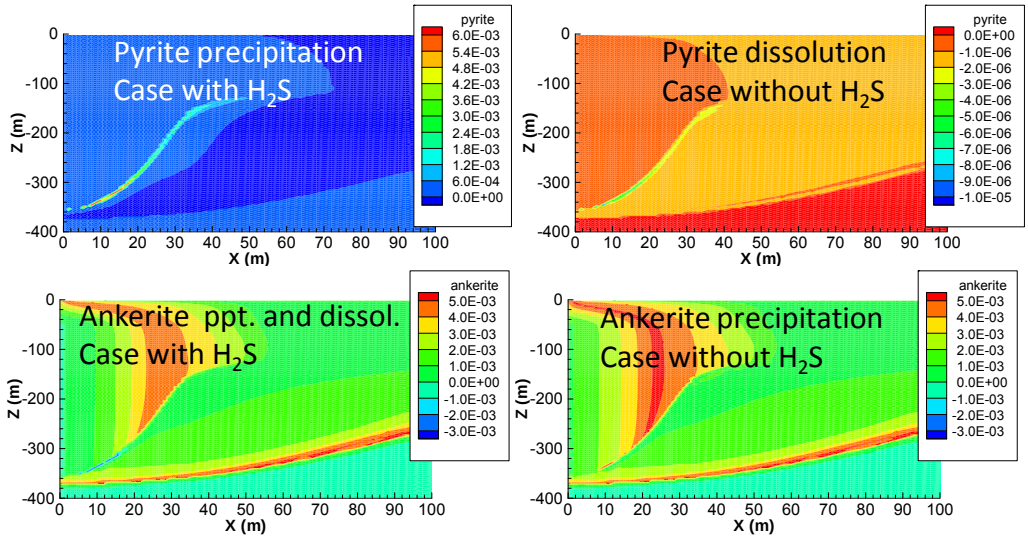

Figure 4-6. *Simulated volume fraction changes for pyrite and ankerite after 40 years. Pyrite dissolves and is replaced by ankerite in the case without H_2S in the injected CO_2. The contours show volume fraction changes (for each individual mineral) that correspond directly to the opposite of absolute changes in porosity.*

Although the maximum predicted porosity change is quite small, the amount of dissolution and precipitation predicted for individual minerals is not negligible. After 40 years of CO_2 injection, Fe-chlorite shows the most absolute volume decrease (~ –1.6 %), and muscovite the most absolute volume increase (~ +0.9%) (Figure 4-7). The main reactions include the replacement of primarily Fe-chlorite by siderite, of calcite by dolomite, and of K-feldspar by muscovite (Figure 4-7). Chalcedony is also predicted to precipitate from the dissolution of feldspars and quartz (volume change up to ~ +0.5%). Because the dissolution of minerals is accompanied by the precipitation of others, the calculated overall porosity change is insignificant.

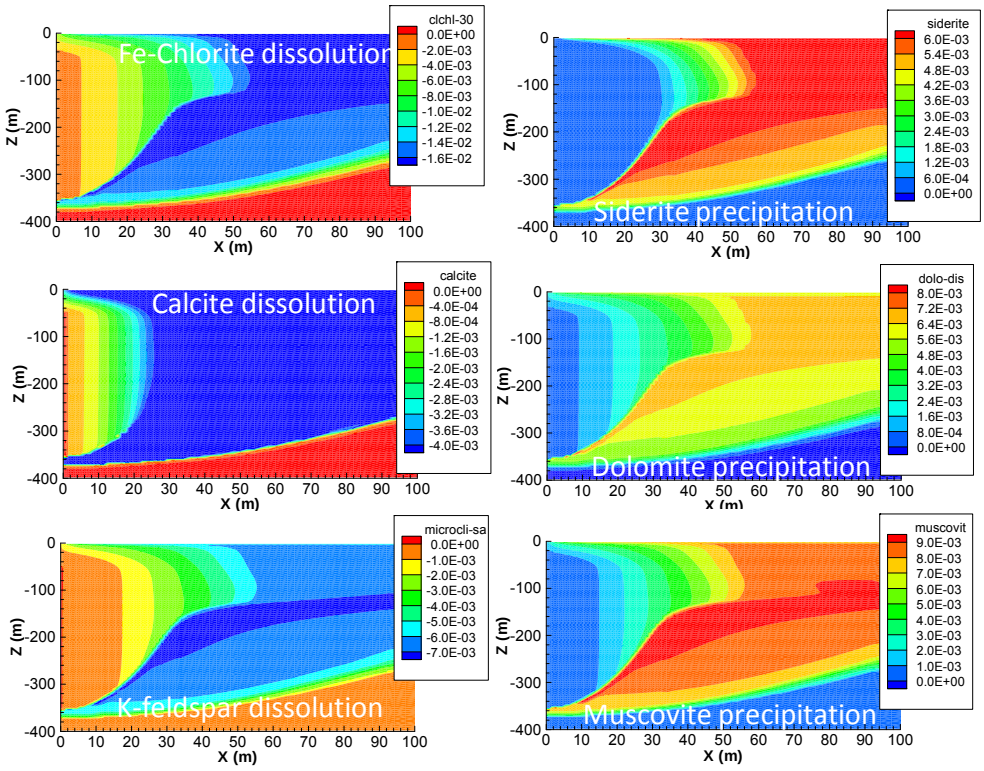

Figure 4-7. *Simulated volume fraction changes for the main reacting minerals after 40 years (case with H_2S in the injected CO_2; the case without H_2S shows similar results for these minerals). The contours show volume fraction changes (for each individual mineral) that correspond directly to the opposite of absolute changes in porosity.*

Other minerals considered in the simulations, including the Hg phase cinnabar, play an insignificant role in the overall predicted porosity change. Glauconite, the only mineral containing Fe(III) in the simulations, affects the distribution of aqueous sulfide (Figure 4-8), because its dissolution frees up Fe(III) which oxidizes sulfide to sulfate. As a result, a zone of aqueous sulfide concentrations below initial background concentrations (~15 micromolal) develops where glauconite dissolves (Figure 4-8).

The effect of H_2S as an impurity in the injected CO_2 is clearly visible on the aqueous sulfide concentration plots (Figure 4-8). The case with H_2S shows a clear band of elevated total aqueous sulfide concentrations directly adjacent to the single-phase CO_2 zone (Figure 4-8, top left). H_2S is quite soluble in water (much more than CO_2), and essentially fully dissolves into the formation water at first contact with water. As a result, the distribution of aqueous sulfide away from the edge of the single-phase CO_2 plume remains similar for the cases with and without H_2S co-injection with CO_2.

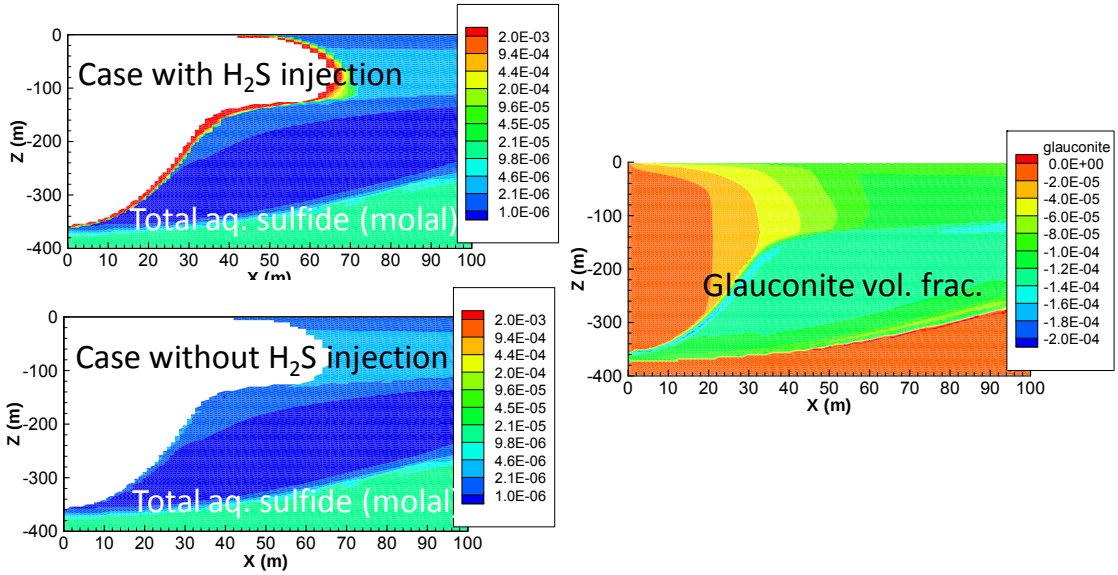

Figure 4-8. *Simulated total aqueous sulfide concentrations (left) after 40 years of CO_2 injection, for cases with and without H_2S included as an impurity (200 ppmV) in the CO_2. The zone of single-phase CO_2 is blanked out (no water present). Aqueous sulfide is oxidized by the dissolution of glauconite (right) resulting in concentrations below background where this mineral dissolves.*

Looking more closely at the Hg behavior, a zone of cinnabar precipitation develops in the vicinity of the injection well (Figure 4-9), with a shape mostly matching the single-phase CO_2 plume. The case with low Hg concentration (7 ppbV) in the CO_2 shows about two orders of magnitude less cinnabar precipitation. In the higher-Hg case, the total amount of Hg input into the system is large (~16 metric tons after 40 years). However, even though essentially this entire amount precipitates as cinnabar, the resulting volume increase as a fraction of formation volume (solid+water) is quite small, and corresponds to an absolute porosity decrease of only about 0.005% (i.e., an insignificant drop from 0.15 to 0.14995) (Figure 4-9, top right). This is because of the high density of this mineral. The reactions leading to cinnanbar precipitation can be written as:

$$Hg(g) \rightarrow Hg(aq)$$
$$\log(K) = -0.95\ (25°C) \text{ and } -2.02\ (100°C) \qquad (4\text{-}1)$$

$$Hg(aq) + 0.25\ SO_4^{-2} + 0.75\ H_2S(aq) + 0.5\ H^+ \rightarrow HgS(s) + H_2O$$
$$\log(K) = 19.83\ (25°C)\ \text{and}\ 16.07\ (100°C) \qquad (4\text{-}2)$$

The dissolved Hg concentrations are quite small (mostly < 8 ppb; Figure 4-9, bottom) because the solubility of cinnabar is quite low. In the higher-Hg case, a thin band of increased concentrations (in the 20 ppb range) develops at the fringe of the single-phase CO_2 plume (Figure 4-9, bottom right), from the formation of Hg-S aqueous complexes that result from the dissolution of H_2S from the CO_2 into the aqueous phase at this location (see Figure 4-8, top left):

$$HgS(s) + 2H_2S_{(aq)} \leftrightarrow HgS(H_2S)_2(aq)$$
$$\log(K) = -4.41\ (25°C)\ \text{and}\ -2.80\ (100°C) \qquad (4\text{-}3)$$

Except for this difference, away from the single-phase CO_2 plume, the distribution of aqueous Hg concentrations in the low- and higher-Hg cases are essentially the same, and are controlled primarily by the cinnabar solubility as a function of aqueous sulfide concentrations and pH (following reaction 4-2), as well as Hg transport in the aqueous phase.

Aqueous sulfide becomes depressed ahead of the single-phase CO_2 plume (from glauconite dissolution, as discussed above; Figure 4-8), and as pH increases away from the CO_2 plume, aqueous $H_2S(aq)$ dissociates to HS^- (around pH ~ 6.5). This causes a somewhat complex distribution of aqueous Hg concentrations, including a thin band of higher concentrations at the bottom of the Hg plume, in both the low- and higher Hg cases (Figure 4-9, bottom). In all cases the aqueous Hg concentrations remain small at all locations.

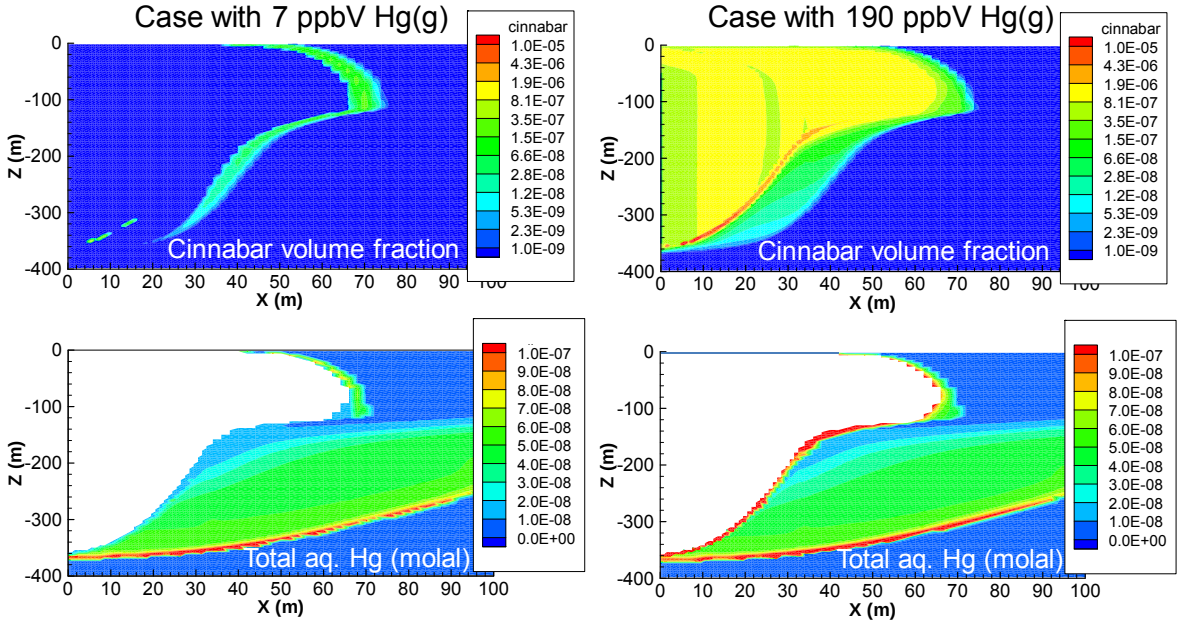

Figure 4-9. *Simulated distribution of cinnabar precipitation (top) and Hg aqueous concentrations (bottom) after 40 years of CO_2 injection. Results are shown for cases with 7 or 190 ppbV Hg, and 200 ppmV H_2S, included as impurities into the CO_2. Volume fraction contours (top) correspond directly to the opposite of absolute changes in porosity. The zone with single-phase CO_2 (no water) is blanked out on the aqueous concentration contour plots (bottom).*

The presence of H_2S in the CO_2 phase affects the distribution of cinnabar precipitation, but only slightly (Figure 4-10). Compared to the case without H_2S, the case with H_2S shows more cinnabar deposition beyond the extent of the single-phase CO_2 plume (Figure 4-10, left), because of the added H_2S from the CO_2 into the formation water. Both cases, however, display about the same maximum amount of cinnabar precipitation (~0.005% of total volume).

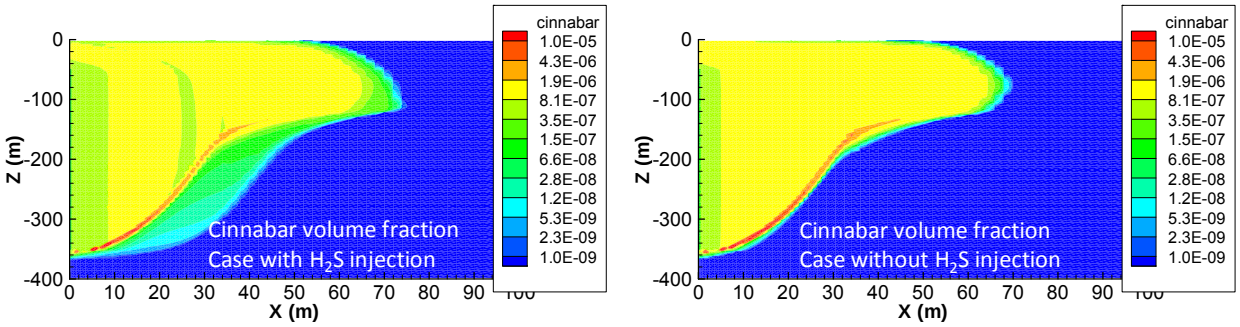

Figure 4-10. *Simulated distribution of cinnabar precipitation after 40 years of CO_2 injection, for cases with 190 ppbV Hg, without and with H_2S (200 ppmV), included as impurities into the CO_2. The contours show volume fraction changes that correspond directly to the opposite of absolute changes in porosity.*

5 EFFECT OF NON-IDEAL BEHAVIOR IN THE CO_2-Hg-H_2O SYSTEM

For all simulations presented in this report, the assumption was made that Hg behaves as an ideal gas. This means that the fugacity of Hg in the gas phase (i.e., the Hg "effective" pressure) is assumed equal to its partial pressure. When computing the Hg phase partitioning, this assumption corresponds to setting the fugacity coefficient equal to one in the relationship

$$K = a_{Hg} / F_{Hg} = a_{Hg} / (\phi P_{Hg}) = \gamma m_{Hg} / (\phi y_{Hg} P_{total}) \quad (5\text{-}1)$$

where K is the equilibrium constant for reaction 4-1 (equivalent to Henry's constant), a stands for activity ("effective" concentration of dissolved Hg), F for fugacity, P for pressure, y for mole fraction in the gas phase, m for molality, γ for activity coefficient, and ϕ for fugacity coefficient. Eq. 5-1 can be recast to express the Hg concentration in the gas phase at equilibrium (as mole fraction y_{Hg})

$$y_{Hg} = \gamma m_{Hg} / (K \phi P_{total}) \quad (5\text{-}2)$$

This relationship shows that if actual values of ϕ were to be less than 1, calculated y_{Hg} values would be higher than when assuming $\phi = 1$. This is the case here, as discussed further below. Therefore, the assumption of ideality tends to underpredict the amount of Hg that can stay in the gas phase, and thus tends to overpredict the amount of Hg that can precipitate from the gas phase.

To quantify this effect, the fugacity coefficient of Hg in a Hg-CO_2 mixture was estimated using the Redlich-Kwong equation of state, with parameters for CO_2 from Spycher et al. (2003), and parameters for Hg estimated from critical properties (Tc = 1764K, Pc = 1670 bar; Huber et al., 2006). Following the same approach as Spycher et al. (2003) for water in CO_2, the fugacity coefficient of Hg in CO_2 was computed by assuming infinite dilution of Hg in the CO_2, which is a good assumption at small Hg concentrations. By this approach, the density of the Hg-CO_2 mixture at elevated temperatures and pressures is assumed to be the same as that of pure CO_2, but the mixing effect of CO_2 on Hg is taken into account in the calculation of the Hg fugacity coefficient. Standard mixing rules were applied, without consideration of specific interaction parameters between Hg and CO_2. Using this approach, calculated fugacity coefficient values of Hg in compressed CO_2 were found to be small, around 0.07 at 106°C and 213 bar. However, it should be noted that the approach followed here is quite approximate, and that the equation of state significantly overestimates the density of pure liquid Hg. Therefore, it is likely that actual fugacity coefficient values would be higher than the values estimated here, but still significantly lower than one, thus suggesting that Hg precipitation could be significantly overestimated when assuming ideal behavior.

As noted in Section 2.4, the numerical simulations did not consider the effect of pressure on the equilibrium constant reflecting the partitioning between aqueous and gaseous Hg (in other words, the effect of pressure on Henry's constant for Hg was neglected). To evaluate this pressure effect, a Poynting factor was estimated as described in Section 2.4. This correction yields a decrease in Hg solubility by about 10% at 106°C and 215 bar (see Figure 2-3) when the equilibrium constant is corrected for pressure. Therefore, ignoring the pressure effect in this case

tends to overestimate the solubility of Hg, which then would underestimate the potential for condensation. However, as seen in Section 2.3, the gaseous Hg concentrations considered here are below saturation (condensation) limits by a factor of at least 10, which is much more than 10% decrease in solubility caused by the pressure correction. This pressure effect is thus not affecting the conclusions reached in this study.

6 SUMMARY AND CONCLUSIONS

A series of modeling investigations was conducted to assess the potential for Hg precipitation (or condensation) from a stream of Hg-containing supercritical CO_2 injected into a sandstone formation at 106°C and 215 bar. Simple calculations were done initially to assess the mass and volume of Hg contaminant that could be deposited in the target formation. These show that any Hg deposition would have to occur on scales of centimeters to potentially affect permeability. These also show that the gaseous Hg contaminant concentrations considered here are well below the concentration level that would be required for condensation, and that evaporative concentration could not yield accumulation of aqueous Hg followed by precipitation.

These calculations were augmented by geochemical and reactive transport modeling investigations. Both types of simulation strongly suggest that cinnabar is expected to precipitate from the CO_2 phase if aqueous sulfide is present in the formation, even in very small concentrations (micromolal range). Sulfide minerals such as pyrite have been identified in the target formation, and sulfide is also projected to be co-injected with CO_2 as an impurity. Therefore, it is anticipated that cinnabar will be deposited around the injection well. Liquid mercury is much less thermodynamically favored than cinnabar when sulfide is present, and would not be expected to condense even in sulfide-free waters at the conditions of interest here (190 ppbV Hg, 106°C, 215 bar), because gaseous Hg concentrations are well below saturation concentrations.

The reactive transport simulations predict that cinnabar will precipitate in the target formation up to about 70 m from the injection well after an injection period of 40 years. The distribution of cinnabar over such a distance from the injection well would not significantly impact porosity (maximum from 0.15 to 0.14995), and therefore would be extremely unlikely to affect permeability. Simulations indicate that a small porosity increase (maximum from 0.15 to 0.1505) is expected ahead of the single-phase CO_2 plume, from (non-Hg) mineral alteration reactions that yield an overall negative volume change. Minor precipitation of (non-Hg) minerals is predicted to take place within the single-phase CO_2 plume (maximum porosity decrease to 0.1495), mostly from evaporative concentrations effects.

All results presented in this report are theoretical in nature, and rely on models and assumptions and various data that all have an inherent uncertainty and/or variability. In absence of experimental data, it is not possible to validate the models applied here. Nevertheless, all the calculation approaches applied in this study suggest that liquid mercury will not form, providing confidence that Hg condensation is not to be expected. However, the precipitation of cinnabar is expected. The modeling using homogenous geochemical and hydrologic properties predicts that deposition will occur over scales of tens of meters, resulting in an insignificant effect on porosity. However, the exact spatial distribution of deposition in the target formation (especially if heterogeneities are considered) remains uncertain, and localized Hg precipitation in some areas cannot be ruled out. This could lead to appreciable porosity reduction, but only if the bulk of the injected Hg precipitates within these areas, over centimeter scales. This is considered unlikely given the long length of injectors (300 m) considered here.

7 ACKNOWLEDGMENT

We thank Tim Kneafsey (LBNL) for helpful discussions of Hg condensation processes and internal review of this report. Support for this work was provided by Chevron with project management by Scott Imbus (Chevron). Additional support was provided by the Assistant Secretary for Fossil Energy (DOE), Office of Coal and Power Systems, through the National Energy Technology Laboratory (NETL), and by Lawrence Berkeley National Laboratory under Department of Energy Contract No. DE-AC02-05CH11231.

8 REFERENCES

Alekseyev, V.A. (2007) Equations for the dissolution reaction rates of montmorillonite, illite, and chlorite. *Geochemistry International* (45)8, 770–780. Original Russian Text in Geokhimiya, 2007, No. 8, pp.842–853.

Altunin, V.V. (1975) Thermophysical properties of carbon dioxide. Moscow: Publishing House of Standards, 551 pp. (in Russian).

Andersson, M.E., Gårdfeldt, K., Wängberg, I., Strömberg, D. (2008) Determination of Henry's law constant for elemental mercury. *Chemosphere,* 73, 587–592.

Arnorsson, S., Stefansson, A. (1999) Assessment of feldspar solubility constants in water in the range 0° to 350°C at vapor saturation pressures. *American Journal of Science*, *299,* (3), 173-209.

Bénézeth, P., Palmer, D.A., Anovitz, L.M., Horita, J. (2007) Dawsonite synthesis and reevaluation of its thermodynamic properties from solubility measurements: Implications for mineral trapping of CO_2. *Geochim. Cosmochim. Acta*, 71, 4438−4455.

Bingham, M.K. (1990) Field detection and implications of Mercury in natural gas. *SPE Production Engineering,* May 1990, 120-124.

Brandt, F., Bosbach, D., Krawczyk-Bärsh, E., Arnold, T., Bernhard, G. (2003) Chlorite dissolution in the acid pH-range: A combined microscopic and macroscopic approach. *Geochimica et Cosmochimica Acta,* 67(8), 1451–1461.

Carroll, S., Mroczek, E., Alai, M., Ebert, M. (1998) Amorphous silica precipitation (60 to 120°C): Comparison of laboratory and field Rates, *Geochimica et Cosmochimica Acta,* 62(8), 1379-1396.

Cui., Z., Aroonwilas, A., Veawab, A., (2010) Simultaneous capture of mercury and CO_2 in amine-based CO_2 absorption Process. *Ind. Eng. Chem. Res.* 49, 12576–12586

Duckworth, O.W., Martin, S.T. (2004) Role of molecular oxygen in the dissolution of siderite and rhodochrosite, *Geochimica et Cosmochimica Acta*, 68(3), 607–621.

Eckersley, N. (2010) Advanced mercury removal technologies. *Hydrocarbon Processing*, 89(1), 29 pp.

Golubev, S.V., Bénézeth, P., Schott, J., Dandurand, J.L., Castillo, A. (2009) Siderite dissolution kinetics in acidic aqueous solutions from 25 to 100°C and 0 to 50 atm PCO_2. *Chemical Geology*, 265, 13–19.

Hellevang, H., Declercq, J., Kvamme, B., Aagaard, P. (2010) The dissolution rates of dawsonite at pH 0.9 to 5 and temperatures of 22, 60 and 77°C. *Appl. Geochem.*, 25, 1575−1586.

Holland, T.J.B., Powell, R. (1998) An internally consistent thermodynamic dataset for phases of petrological interest. *J. Met. Geol.,* (16) 309–343.

Holman, G.J.F., ten Seldam, C.A. (1994) A critical evaluation of the thermophysical properties of mercury. *J. Phys. Chem. Ref. Data*, 23, 5, 807-827.

Huber, M.L., Laesecke, A., Friend, D.G. (2006) The Vapor Pressure of Mercury. Report NISTIR 6643, National Institute of Standards and Technology, Boulder, CO 80305-3328, 56pp.

Johnson, J.W, Oelkers, E., Helgeson, H.C. (1992) SUPCRT92: A software package for calculating the standard molal thermodynamic properties of minerals, gases, aqueous species and reactions from 1 to 5000 bar and 0 to 1000°C. *Comput Geosci*, (18) 899–947.

Joseph, B., Picat, M., Barbier, F. (1999) Liquid metal embrittlement: A state-of-the-art appraisal. *Eur. Phys. J. AP* 5, 19-31.

Lasaga, A.C., Soler, J.M., Ganor, J., Burch, T.E., Nagy, K.L. (1994) Chemical weathering rate laws and global geochemical cycles. *Geochimica et Cosmochimica Acta,* 58, 2361–2386.

Markovs J., Clark K. (2005) Optimized mercury removal in gas plants. Proceedings of the 8th Annual Gas Processors Association Convention, San Antonio, Texas. https://www.gpaglobal.org/publications/view/id/930/

NIST (2011) NIST Chemistry Web Book, NIST Standard Reference Database Number 69, June 2011 Release [online]. Available from: http://webbook.nist.gov/chemistry.

Oldenburg, C.M., Moridis, G.J., Spycher, N., Pruess, K. (2004) EOS7C Version 1.0: TOUGH2 Module for Carbon Dioxide or Nitrogen in Natural Gas (Methane) Reservoirs, Lawrence Berkeley National Laboratory Report *LBNL-56589*, March 2004.

Palandri, J., Kharaka, Y.K. (2004) A compilation of rate parameters of water–mineral interaction kinetics for application to geochemical modeling, US Geol. Surv. Open File Report 2004-1068, 64 pp.

Palandri, J., Reed, M.H. (2001) Reconstruction of in situ composition of sedimentary formation waters. *Geochimimica et Cosmochimica Acta* (65) 1741–1767.

Pruess, K., Müller, N. (2009) Formation dry-out from CO_2 injection into saline aquifers: 1. Effects of solids precipitation and their mitigation. *Water Res. Research*, 45, W03402, doi:10.1029/2008WR007101.

Pruess, K., Spycher, N. (2007) ECO2N – A Fluid property module for the TOUGH2 code for studies of CO_2 storage in saline aquifers. *Energy Conversion and Management*, 48 (6), 1761-1767.

Pruess, K., C.M. Oldenburg and G.J. Moridis. TOUGH2 User's Guide Version 2. E. O. Lawrence Berkeley National Laboratory Report *LBNL-43134*, 1999; and *LBNL-43134* (revised), 2011.

Reed M. H., Spycher N.F. (1984) Calculation of pH and Mineral Equilibria in Hydrothermal Waters with Application to Geothermometry and Studies of Boiling and Dilution. *Geochimica et Cosmochimica Acta*, 48, 1479-1492.

Reed, M.H. (1982) Calculation of multicomponent chemical equilibria and reaction processes in systems involving minerals, gases and an aqueous phase. *Geochimimica et Cosmochimica Acta*, 46, 513–528.

Reed, M.H. (1998) Calculation of simultaneous chemical equilibria in aqueous-mineral-gas systems and its application to modeling hydrothermal processes. In: Techniques in Hydrothermal Ore Deposits Geology, Reviews in Economic Geology, Volume 10. Richards J, Larson P (eds), 109–124.

Reed, M.H., Palandri, J. (2006) SOLTHERM.H06, a database of equilibrium constants for minerals and aqueous species. Available from the authors, University of Oregon, Eugene, Oregon.

Sonnenthal, E.L., Spycher, N., Xu, T., Zheng, L., Miller, N.L., and Pruess, K. (2014) TOUGHREACT V3.0-OMP Reference Manual: A Parallel Simulation Program for Non-Isothermal Multiphase Geochemical Reactive Transport, LBNL Report in preparation. http://esd.lbl.gov/research/projects/tough/software/toughreact.html

Spycher, N., Peiffer, L., Saldi, G., Sonnenthal, E., Reed, M.H., Kennedy, B.M. (2014) Integrated multicomponent solute geothermometry. *Geothermics* 51, 113–123.

Spycher, N., Peiffer, L., Sonnenthal, E. (2013) GeoT User's Guide A Computer Program for Multicomponent Geothermometry and Geochemical Speciation Version 1.4. Lawrence Berkeley National Laboratory, Report No. *LBNL-6172E*. (http://esd.lbl.gov/research/projects/geot/)

Spycher, N., Pruess, K., Ennis-King, J. (2003) CO_2-H_2O Mixtures in the Geological Sequestration of CO_2. I. Assessment and calculation of mutual solubilities from 12 to 100°C and up to 600 bar. *Geochim. Cosmochim. Acta, 67, 3015-3031.*

Spycher, N.F., Reed, M.H. (1989) Evolution of a Broadlands-type epithermal ore fluid along alternative P-T paths: implications for the transport and deposition of base, precious, and volatile metals. *Economic Geology*, 84, 328-359.

Tardy, Y., Fritz, B. (1981) An ideal solid solution model for calculating solubility of clay minerals. *Clay Minerals*, 16, 361-373.

Wagner, W., Pruss, A. (2002) The IAPW formulation 1995 for the thermodynamic properties of ordinary water substance for general scientific use. *J. Phys. Ref. Data*, **31**, 387–535.

Weatherford Laboratories (2011) Using Gas Geochemistry to Assess Mercury Risk. http://www.gaschem.com/mercur.html

Xu, T., Spycher, N., Sonnenthal, E., Zhang, G., Zheng, L., Pruess, K. (2011) TOUGHREACT Version 2.0: A simulator for subsurface reactive transport under non-isothermal multiphase flow conditions. *Computers & Geosciences*, 37, 763–774.

Yang, L., Steefel, C.I. (2008) Kaolinite dissolution and precipitation kinetics at 22 °C and pH 4. *Geochimica et Cosmochimica Acta*, 72, 99–116.

Zettlitzer, M., Schöler, H.F., Eiden, R., Falter, R. (1997) Determination of elemental, inorganic and organic mercury in North German gas condensates and formation brines. SPE 37260, *Proceedings of the Internatioal Symposium on Oil Field Chemistry*, Houston, Texas, February 18-21, 509- 516.